CHEMISTRY OF MATERIALS

pubs.acs.org/cm

Article

Magnetoelastic Coupling and Cryogenic Magnetocaloric Effect in Two-Site Disordered $GdSrCoFeO_6$ Double Perovskite

Romualdo S. Silva, Jr, Javier Gainza, Cledson dos Santos, João Elias F. S. Rodrigues, Catherine Dejoie, Yves Huttel, Nevenko Biskup, Norbert M. Nemes, José Luis Martínez, Nilson S. Ferreira, and José Antonio Alonso*

Cite This: *Chem. Mater.* 2023, 35, 2439−2455

Read Online

ACCESS | Metrics & More | Article Recommendations | Supporting Information

ABSTRACT: The development of new magnetic refrigerants demands an effective investigation of materials with a large magnetocaloric effect in a wide temperature range. Herein, we report on the structural, magnetic, and magnetocaloric properties of the two-site disordered double perovskite $GdSrCoFeO_6$ prepared by the modified solid-state synthesis method. Temperature-dependent synchrotron X-ray diffraction analysis revealed that $GdSrCoFeO_6$ crystallizes in the orthorhombic phase (*Pnma*), with Gd^{3+}/Sr^{2+} and $Co^{2+/3+}/Fe^{3+/4+}$ ions randomly distributed on the A- and B-sites, respectively. An observed lattice parameter anomaly around 60 K indicates the occurrence of the magnetoelastic coupling, which coincides with the presence of ferro/ferrimagnetic (FM/FiM) ordering below $T_C \approx 65$ K from the magnetic measurements. These results match well with our first-principles calculation prediction of low-temperature magnetic (FM/FiM) and electronic (insulating/metal) transitions related to a combined effect of Co and Fe short- and long-range competitions, crossings of spin state at Co ions, and the hybridization degree between Gd-4*f* and Co-3*d* states. Additionally, a modified Arrott plot and Kouvel−Fisher analysis were used to establish the nature of the magnetic phase transition in $GdSrCoFeO_6$, yielding the critical exponent $\beta = 1.46(6)/1.45(6)$, $\gamma = 1.48(5)/1.17(2)$, and $\delta = 2.01(3)/1.80(5)$, respectively. The specific heat analysis reveals two well-defined broad peaks (~10 and ~70 K), which match well with a Schottky anomaly (Gd-4*f*) and the magnetic transition of FM/FiM to paramagnetic order, respectively. The magnetocaloric effect (MCE) analysis reveals a maximum magnetic entropy change $\Delta S_M^{max} \approx 13$ J kg^{-1} K^{-1} (at ~8 K) under a field of 0−7 T. These results evidence that the Schottky anomaly and the magnetoelastic coupling seem to be key factors for driving further enhancements to the MCE in $GdSrCoFeO_6$, making it a possible candidate for cryogenic applications.

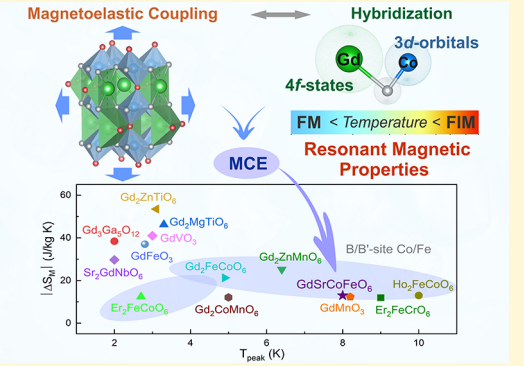

1. INTRODUCTION

Magnetic refrigeration (MR) was proposed in the late 1920s through thermodynamic studies and based on adiabatic demagnetization cooling at very low temperatures.[1] Upon applying or removing an external magnetic field to a magnetic material, an isothermal change of magnetic entropy (ΔS_M) takes place, which is phenomenologically known as the magnetocaloric effect (MCE).[2] The overall efficiency of the MCE can reach up to 60% of the theoretical Carnot cycle, making MR a promising energy-efficient and environmentally friendly technology.[3,4] The magnitude of the MCE is closely related to the coupling of the magnetic field with the magnetic sublattice, which peaks around the magnetic transition of ordering (T_C/T_N). Thus, MCE investigation can also provide valuable information to understand the magnetic transition interactions of the materials.[5] The progress in MR technologies also requires magnetocaloric materials with compositions at the critical point of second-order phase transition (SOPT), since first-order phase transition materials have limited cyclability.[6,7] In this way, many studies have been dedicated for discovering and developing new materials exhibiting an appropriate MCE at different working temperatures.[2,4,8−11] On the other hand, a gap exists between the performance and MR practical application for magnetic solids, where finding suitable materials with promising performance is one of the most important tasks. It is worth stressing that adequate characterization of these materials is crucial in assessing their applicability.[12]

Recently, rare earth (RE)-based materials with highly localized 4*f* orbitals have been widely studied as possible candidates for MCE materials due to their large magnetic

Received: November 30, 2022
Revised: February 23, 2023
Published: March 8, 2023

moment. Among these, we can mention the intermetallic compounds, double perovskite oxides, alloys, and sulfides, among others.[9,13−16] Notably, double perovskites (DP) with chemical formula $AA'BB'O_6$ have drawn attention because their crystal structure may accommodate different elements in both sites (AA', BB'), which provides a variety of interesting and potentially useful properties. They can play a vital role due to their physical properties, for instance, catalytic activity, electronic and ionic conductivity, chemical stability, and magnetic ordering, among others.[17] These perovskites may crystallize in the monoclinic ($P2_1/n$—ordered) or orthorhombic (*Pnma*—disordered) space groups, depending on the charge and size differences of the elements residing on both sites.[3,5,18−22] In these tilted octahedral systems, some AA'−O distances become smaller, thus optimizing the AA'−O bonds for small AA' cations, while some become longer, reducing the effective coordination environment. On the other hand, the $[BB']O_6$ octahedra are distorted upon octahedral rotation to a greater or lesser degree, which can be due to purely steric effects and electronic factors associated with certain electronic configurations of the BB' transition metals.[23] Such a panoply of characteristics can lead to several noncentrosymmetric structures due to the possible combinations of valences of the AA' and BB' cations, such as 2+/2+, 2+/3+, 3+/3+, 3+/4+, and 4+/4+, respectively.[24]

Recent results have shown that DP containing Gd, such as Gd_2ZnTiO_6,[3] Sr_2GdNbO_6,[5] $(Ba,Sr,Ca)_2GdSbO_6$,[14] and Gd_2MgTiO_6,[18] present promising magnetocaloric properties yielding values of ΔS_M around 26.1−53.5 J/kg K (for magnetic fields in the range of 0−9 T). This can be associated with the spin-glass behavior as well as with rare earth sublattices with antiferromagnetic (AFM) interactions at low temperatures. On the other hand, DP containing Co/Fe into the BB' site, for instance, $(Er,Gd,Ho)_2FeCoO_6$,[25,26] can exhibit FM order in the structure and enhance the MCE in a wide temperature range, with ΔS_M and the relative cooling power (RCP) around 13−22 J/kg K and 280−346 J/kg (for magnetic fields in the range of 0−7 T), respectively. They outperform other DP compounds with different transition metals in the BB' site, such as $(Gd,Dy,Ho)_2(Cu,Cr,Ni)MnO_6$ with $\Delta S_M \sim 7.8$−9.2 J/kg K and RCP ∼ 122−160 J/kg.[27,28] The final features of the magnetically frustrated materials may be manipulated according to the degree of disorder and/or vacancies within their crystal structure. Such phenomena can be directly linked to magnetoelastic coupling, i.e., when the deviation of the lattice parameters from a monotonic behavior occurs, in the presence of a magnetic lattice, with temperature. A detailed study of such a structural property is essential to find new candidates with high magnetocaloric efficiency.[14,29,30]

In this work, we report the structural, electronic, and magnetic studies of the disordered double perovskite $GdSrCoFeO_6$ deduced from a combination of X-ray diffraction, synchrotron X-ray diffraction, Rietveld refinement, specific heat, magnetocaloric effect, dc and ac magnetization measurements, and density functional theory (DFT) calculations. Structural studies reveal that $GdSrCoFeO_6$ crystallizes in the orthorhombic *Pnma* space group in which Gd^{3+}/Sr^{2+} and $Co^{2+/3+}/Fe^{3+/4+}$ ions are randomly distributed at the AA' and BB' sites, respectively. Magnetization measurements suggested the presence of predominantly ferro/ferrimagnetic and superexchange interactions due to antisite disorder, although Gd^{3+} ions mainly contribute to the magnetism. The MCE analysis reveals a maximum magnetic entropy change $\Delta S_M^{max} \approx 13$ J kg^{-1} K^{-1} under a field of 0−7 T, which can be an alternative for cryogenic magnetocaloric applications toward the working temperature range of hydrogen liquefaction.

2. METHODOLOGY

2.1. Sample Preparation. The $GdSrCoFeO_6$ double perovskite has been synthesized by the modified solid-state method using high-purity Gd_2O_3 (99.99%, ROC), $SrCO_3$ (Merck), Co_2O_3 (99.999%, Merck), and Fe_2O_3 (99%, Merck) as metal source materials. First, the precursors were mixed in a proper stoichiometric ratio 1:1:1:1 (Gd:Sr:Co:Fe) and ground in a mortar and pestle. Then, the mixture was set into and sealed in a zirconia-lined jar together with 30 zirconia balls (of 5 mm diameter) and conducted out in a Retsch PM100 Planetary ball mill (Haan, Germany) at 450 rpm for 2 h. Finally, the powder (∼1 g) was calcined at 1300 °C for 6 h in an air atmosphere.

2.2. Structural Characterization and Analysis. Initial-phase characterization was carried out using X-ray diffraction (XRD) on a Bruker-AXS D8 diffractometer (40 kV, 30 mA), run by the DIFFRACTPLUS software, in Bragg−Brentano geometry with Cu Kα radiation (λ = 1.5418 Å). The synchrotron X-ray diffraction (SXRD) data were recorded at the ESRF beamline ID22 (Grenoble, France) operating at a wavelength of λ = 0.35418 Å (∼35 keV). The $GdSrCoFeO_6$ sample was sealed in a quartz-glass capillary of 0.5 mm diameter and measured under rotation to minimize potential texture effects. The X-ray energy of 35 keV was chosen to minimize absorption effects. The high-resolution powder diffraction patterns were collected over the range 1−40° (2θ) in continuous scanning mode for temperatures ranging from 6 to 300 K with a 15 min waiting time at each temperature step in order to guarantee an isothermal condition. SXRD patterns were retrieved following the processing method described in ref 31. XRD and SXRD patterns were analyzed by Rietveld refinement using the *FullProf* program.[32] The peak shape was described using a pseudo-Voigt function, and the background interpolated between areas devoid of reflections. The full refinement included the following parameters: scale factors, zero-point error, background coefficients, asymmetry correction factors, lattice parameters, atomic positions, occupancy factors, and isotropic displacement parameters.

2.3. Surface Chemistry and Analysis. Core-level X-ray photoelectron spectroscopy (XPS) data were acquired in a chamber with a base pressure of 10^{-10} mbar using a hemispherical electron energy analyzer (SPECS Phoibos 100 spectrometer) and an X-ray source at Al Kα (1486.29 eV). The powder samples were deposited onto clean and conductive double-side carbon tape, loaded in a vacuum load-lock chamber, and finally transferred to ultrahigh vacuum. No cleaning protocol with argon bombardment was considered in order to avoid Ar^+-induced electronic changes (in particular in oxides). The XPS data were recorded using an Al laboratory anode operated at moderate power (150 W). Under such conditions, beam-induced reduction or changes are not expected in nonorganic compounds. The angle between the hemispherical analyzer and the plane of the surface was kept at 60°. The survey spectrum was recorded with a resolution of 0.5 eV and a pass energy of 40 eV. Specific core-level spectra (Gd 4*d*, Sr 3*d*, Co 2*p*, Fe 2*p*, O 1*s*, and C 1*s*) were acquired with an energy resolution of 0.1 eV and a pass energy of 20 eV.

https://doi.org/10.1021/acs.chemmater.2c03574
Chem. Mater. 2023, 35, 2439−2455

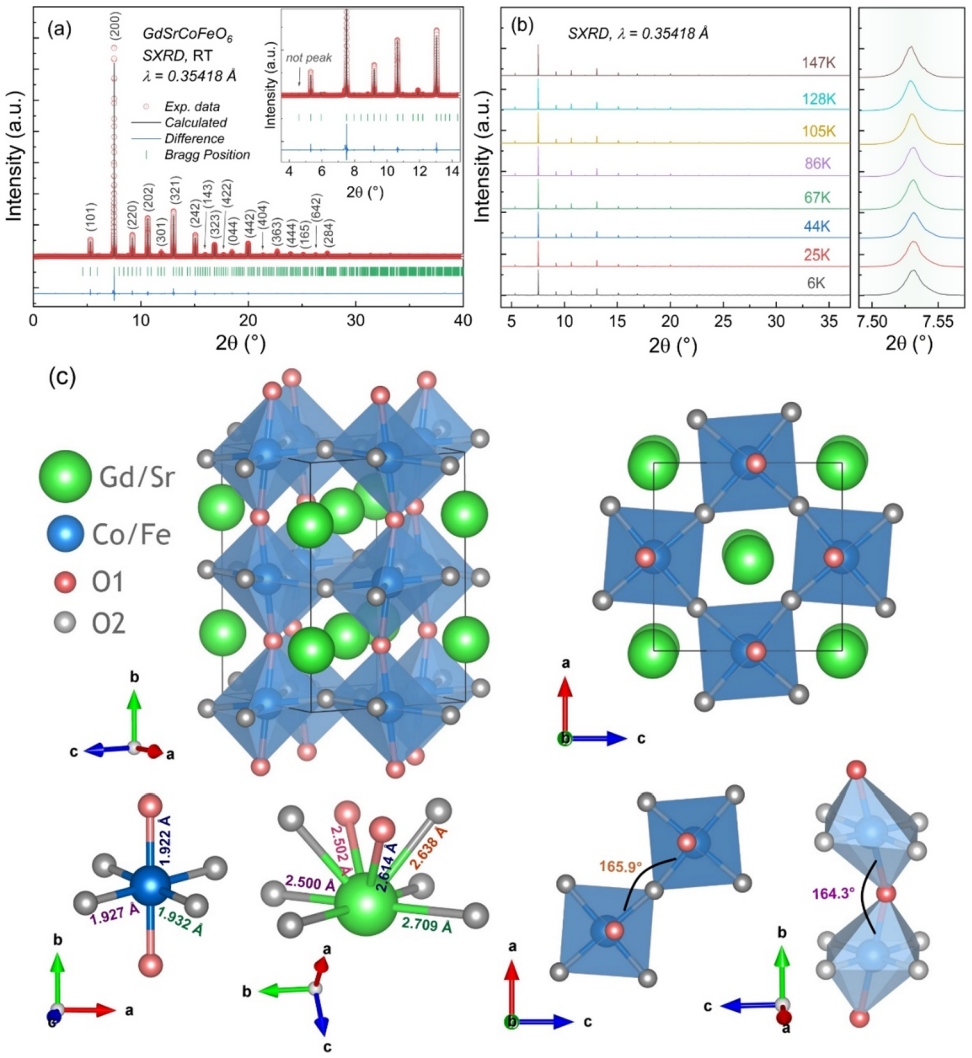

Figure 1. (a) SXRD Rietveld refinement plots at room temperature for the $GdSrCoFeO_6$ double perovskite. Experimental data (red circles), calculated profile (black line), difference (blue line), and Bragg position (green vertical lines). (b) SXRD pattern collected in the temperature range of 6−147 K. (c) Detailed local crystalline structure of disordered $GdSrCoFeO_6$ coordinated by octahedra with their corresponding interatomic distance variations and bond angle distortions.

Data processing was performed within the *CasaXPS* software, and the absolute binding energies were adjusted to the binding energy reference to the C 1*s* core level at 285 eV.[33] Peak areas were obtained by fitting the spectra and relative sensitivity factors from the atomic photoionization cross section of each core level provided by the SPECS Prodigy library. In all the fittings for Sr 3*d*, G*d* 4*d*, Co 2*p*, and Fe 2*p*, we tried to constrain the peak area and widths according to the respective multiplet theory. The peak positions were defined as free parameters, converging in somehow that the separation agreed with literature results (NIST XPS database). For Sr, Gd, and Fe, the area constraints worked quite well from which the surface valence states for those elements were estimated. For Co 2*p*, the convergence was only reached after including (1) the spin-orbit doublets for Co^{3+} with $Ap_{1/2}/Ap_{3/2} \sim 0.4$; (2) the doublets for Co^{2+} with $Ap_{1/2}/Ap_{3/2} \sim 0.3$; (3) two satellite peaks at 787.5 ($p_{3/2}$) and 805.5 ($p_{1/2}$) eV. For the doublets, the widths were kept almost equal ($\gamma_{3/2} \sim \gamma_{1/2}$).

2.4. Transmission Electron Microscopy. Scanning transmission electron microscopy (STEM) was carried out in a JEOL ARM 200 electron microscope operated at 200 kV. The microscope is equipped with a Gatan Quantum electron energy loss spectrometer (EELS). The EELS spectra are denoised by the principal component analysis software.

2.5. Magnetic and Transport Properties. The magnetic properties were measured with a SQUID magnetometer (MPMS-3), from Quantum Design (San Diego, USA) in a temperature range from 1.8 up to 300 K and a range of magnetic fields up to 7 T. The ac susceptibility was measured in a PPMS Quantum Design (San Diego, USA) with the ac susceptometer in a frequency range from 100 Hz up to 10 kHz, with an oscillatory field with an amplitude of 1 Oe. The samples were also measured in different external magnetic fields of H = 0.0, 0.05, 0.5, and 1.5 T under a fixed frequency of 10 Hz. The heat capacity was also measured in the PPMS with an adiabatic heat pulse method. For this, the ceramic pellets were cut with a diamond saw to fit into the sample-holder dimensions.

2.6. Computational Details. DFT[34,35] calculations for $GdSrCoFeO_6$ were performed using the WIEN2k code[36] and the full-potential linearized-augmented-plane-wave method.[37] The suitable radii R_{Mt} of the muffin-tin sphere were 2.36, 2.15, 1.85, 1.90, and 1.56 atomic units (a.u.) for Gd, Sr, Co, Fe, and O, respectively. Electronic waves were expanded up to l_{max} = 10

https://doi.org/10.1021/acs.chemmater.2c03574
Chem. Mater. 2023, 35, 2439−2455

Table 1. Structural Parameters of $GdSrCoFeO_6$ Determined by Rietveld Refinement of SXRD Data at Room Temperature

crystallographic data					
atom	Wyck. Posit.	x	y	z	lattice parameters (Å)
Gd/Sr	4*c*	0.5154(2)	0.25	0.4942(9)	a = 5.4003(1)
Co/Fe	4*b*	0.50	0.00	0.00	b = 7.6300(3)
O1	4*c*	−0.0030(3)	0.25	0.5436(2)	c = 5.4094(2)
O2	8*d*	0.2693(1)	0.0285(1)	0.7301(1)	V = 222.89(3) Å^3
reliability factors: R_p = 6.71%, R_{wp} = 8.82%, R_{exp} = 2.11%, R_{Bragg} = 3.42%, χ^2 = 16.8					
bond lengths (Å) and angles (°)					
(Co/Fe)−O1 (Å)		(Co/Fe)−O2 (Å)		(Gd/Sr)−O1 (Å)	(Gd/Sr)−O2 (Å)
1.922(1)		1.932(5)		2.614(4)	2.709(4)
		1.927(5)		2.502(6)	2.638(5)
					2.500(1)
⟨(Co/Fe) − O⟩ = 1.927(4)				⟨(Gd/Sr) − O⟩ = 2.592(9)	
(Co/Fe)−O1−(Co/Fe) (°)				(Co/Fe)−O2−(Co/Fe) (°)	
164.3(3)				165.9(4)	
⟨(Co/Fe) − O − (Co/Fe)⟩ = 165.1(4)					

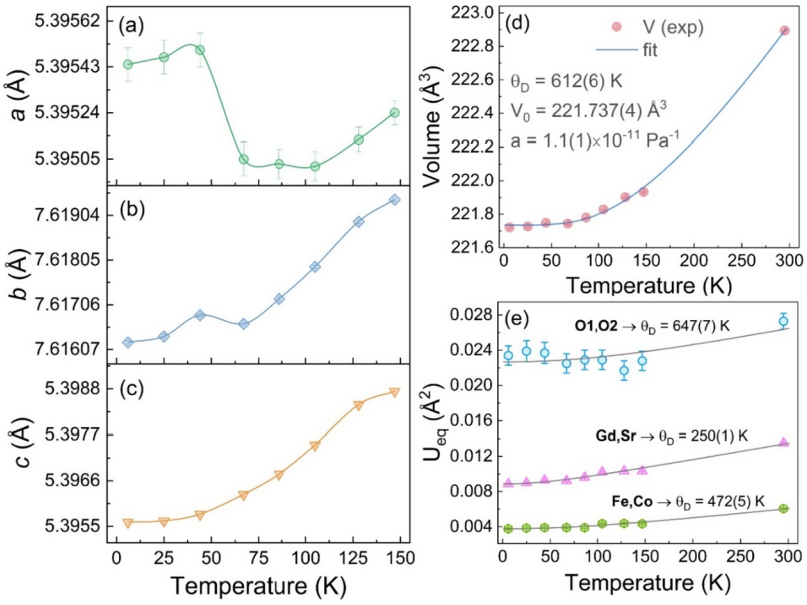

Figure 2. Temperature variations of lattice parameters *a*, *b*, *c*, and volume (V) are shown in (a), (b), (c), and (d), respectively. (e) Experimental $U_{eq}(T)$ values extracted from the Rietveld refinement together with the fitting provided by eq 2.

within the atomic spheres, while the cut-off limited plane waves are in the interstitial region at $k_{max} = 7.0/R_{MT}(O)$. The charge density was Fourier expanded up to $G_{max} = 12$. Band structure calculations were carried out with a suitable *k*-mesh of 6 × 6 × 6 *k*-points in the Brillouin zone. For the exchange-correlation description, we apply the GGA + U scheme, which combines PBEsol parametrization[38] and the Hubbard model. We consider the U_{eff} = U-J effective potential term in accordance with the method by Anisimov et al.[39] After testing different values for the Hubbard U_{eff} parameter, we use 6.0 eV to describe the Gd-4*f* strong correlated electrons and 4.0 eV for the 3*d*-states of Co and Fe ions. The choice of the GGA + U beyond DFT standard calculations was motivated by our successful description of the structural, magnetic, and electronic characteristics of $NdSrCoFeO_6$.[40] The calculations were successfully converged in energy (10^{-5} Ry) and charge (10^{-5} eV/bohr^3) criteria, and the relaxation process of the internal parameters ended when the forces between the atoms were less than 2mRy/bohr.

3. RESULTS AND DISCUSSION

3.1. Structural and Surface Chemistry Characterization. The XRD pattern of $GdSrCoFeO_6$ double perovskite has been acquired at room temperature and indexed to the orthorhombic symmetry with *Pnma* (#62) space group (ICSD #154063), and the Rietveld refinement is shown in Figure S1 (Supplementary Information - SI). No impurity peaks have been observed within the instrument's resolution limit. Afterward, the SXRD patterns were collected in the 6−300 K temperature range. The pattern collected at room temperature was again indexed and confirmed the orthorhombic symmetry in the *Pnma* (#62) space group. The *hkl* indices and final Rietveld refinement at room temperature are illustrated in Figure 1a with the main crystallographic results listed in Table 1, which indicates a good agreement between the refined and the experimental SXRD patterns. The inset of Figure 1a illustrates the profile fit for the reflections between ∼4 and ∼14°. No apparent peak before $2\theta \approx 5°$ was observed (as well as at $2\theta \approx 20°$ in the inset of Figure S1), discarding any Co/Fe

https://doi.org/10.1021/acs.chemmater.2c03574
Chem. Mater. 2023, 35, 2439−2455

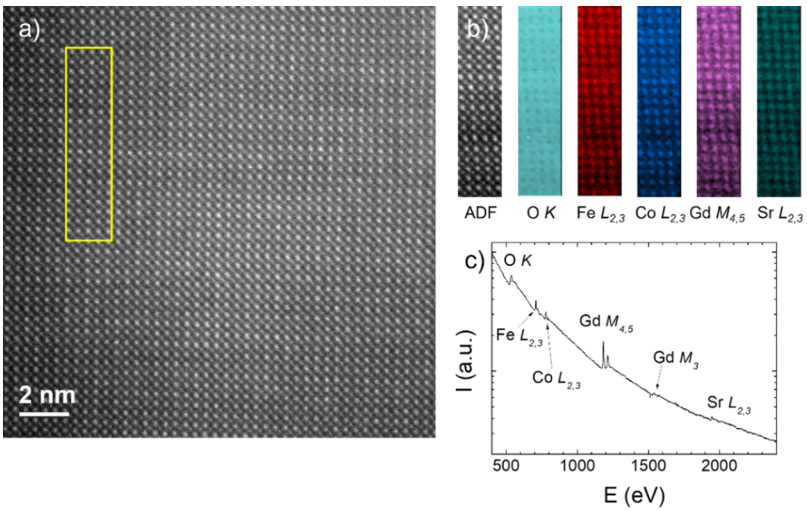

Figure 3. (a) Part of the crystal where EELS data are taken (yellow rectangle). (b) Simultaneous ADF image and elemental maps based on the oxygen *K*, iron, cobalt $L_{2,3}$, gadolinium $M_{4,5}$, and strontium $L_{2,3}$ edge. (c) EELS edges are used for the elemental maps.

long-range ordering in the crystalline structure.[19,41] In fact, in the orthorhombic *Pnma* space group, long-range ordering of the Co/Fe ions in the octahedral *B*/*B*′ sites not is allowed. A trial fit in the monoclinic $P2_1/n$ space group (see Figure S2), where Fe and Co ions would be long-range ordered, since they are located in different crystallographic 2*a* and 2*b* sites, did not yield any improvement over the disordered *Pnma* model. Therefore, in the orthorhombic model for the $GdSrCoFeO_6$ structure, Gd/Sr cations and O1 anions occupy the 4*c* (*x*,1/4,*z*) sites, whereas the Co/Fe cations are randomly distributed at the 4*b* (1/2,0,0) sites. The 8*d* (*x*,*y*,*z*) general position is occupied by O2 anions.

Figure 1c displays a view of the crystal structure of $GdSrCoFeO_6$ generated by the VESTA[42] software. The bond lengths and angles for $GdSrCoFeO_6$ are also included in Table 1. The obtained values of the lattice parameters a = 5.4003(1) Å, b = 7.6300(3) Å, c = 5.4094(2) Å, and V = 222.89(3) Å^3, the average bond length ⟨(Co/Fe) − O⟩ = 1.927(4) Å and ⟨Gd/Sr − O⟩ = 2.592(9) Å, and the average bond angle ⟨(Co/Fe) − O − (Co/Fe)⟩ = 165.1(4)° agree with those obtained for other DP with an orthorhombic structure.[21,43,44] Comparatively, the $GdSrCoFeO_6$ disordered structure is less distorted because the Gd ionic radius is smaller compared to Pr and La ions (r_{Gd} = 1.05 Å < r_{Pr} = 1.13 Å < r_{La} = 1.16 Å), for example, and despite *A*-site sharing with Sr (with a larger radius, r_{Sr} = 1.26 Å), a cell volume reduction is caused through bond lengths decreasing, whereas the bond angles increase. To better visualize this, the octahedral tilting can be calculated through the expression Φ = [180 − ⟨(Co/Fe) − O − (Co/Fe)⟩]/2,[22] resulting in Φ = 7.5° and indicates a slight octahedral tilting.

The magnetoelastic coupling in the $GdSrCoFeO_6$ double perovskite was investigated by temperature-dependent SXRD patterns collected in the 6−147 K temperature range, as shown in Figure 1b. No additional peaks or peak splitting was detected in the entire temperature interval. All the SXRD data were satisfactorily refined with *Pnma* symmetry, thus ruling out any global structural transition down to 6 K (see the SXRD Rietveld refinement plot at 6 K in Figure S3 of the SI). The temperature variations of the lattice parameters *a*, *b*, *c*, and volume (*V*) derived from the refinement Rietveld analysis showed a pronounced anomaly near $T \approx 70$ K (see Figure 2a−d), mainly for the *a*-lattice parameter. The *a*-lattice parameter tends to slightly increase between 6 and 40 K and then has a pronounced decrease of −0.0003(9) Å until 70 K, whereas *b*- and *c*-lattice parameters increase by +0.0004(1) and +0.0006(7) Å, respectively. Above 70 K, they all respectively increase by +0.0001(9), +0.0027(5), and +0.0024(7) Å up to 147 K. Consequently, a significant thermal expansion of +0.5(2)% in the volume (ΔV = 1.1(5) Å^3) is observed from 70 up to 300 K (see Figure 2d). Probably, this anomaly in the lattice parameters is associated with a local atomic rearrangement, which coincides very well with the magnetic order transition of $GdSrCoFeO_6$ at $T_C \approx 65$ K (as discussed later). Therefore, this behavior may be attributed to a possible magnetoelastic coupling observed for the $GdSrCoFeO_6$ sample. On the other hand, this requires further investigation, which is, however, out of the scope of this paper.

The thermal expansion of the unit-cell volume was treated using the Grüneisen approximation to the zero-pressure equation of state according to its first-order expansion, as follows:[45]

$$V(T) = V_0 + \frac{9\gamma N k_B T}{B_0}\left(\frac{T}{\theta_D}\right)^3 \int_0^{\theta_D/T} \frac{x^3 dx}{e^x - 1} \quad (1)$$

where V_0 denotes the unit-cell volume at 0 K, θ_D the Debye temperature, N the number of atoms in the unit cell, B_0 the isothermal bulk modulus, and γ the Grüneisen parameter. Figure 2d compares the experimental volume expansion and the fitted line using eq 1. The fitting provided V_0 = 221.737(4) Å^3, θ_D = 612.589 K, and $\gamma/B_0 = 1.11 \times 10^{-11}$ Pa^{-1}. The Debye temperature of $GdSrCoFeO_6$ has a similar value to those found in the literature for $CaGeO_3$[46] and $BaZrO_3$;[47] both are also derived from volume thermal expansion. Additionally, the individual atomic oscillations can be accessed using the mean square displacements (MSDs or U_{eq} in units of Å^2),[48] as described by:

$$U_{eq}(T) = d_s^2 + \frac{3\hbar^2 T}{m k_B \theta_D^2}\left[\frac{T}{\theta_D}\int_0^{\theta_D/T} \frac{z}{e^z - 1} dz + \frac{\theta_D}{4T}\right] \quad (2)$$

https://doi.org/10.1021/acs.chemmater.2c03574
Chem. Mater. 2023, 35, 2439−2455

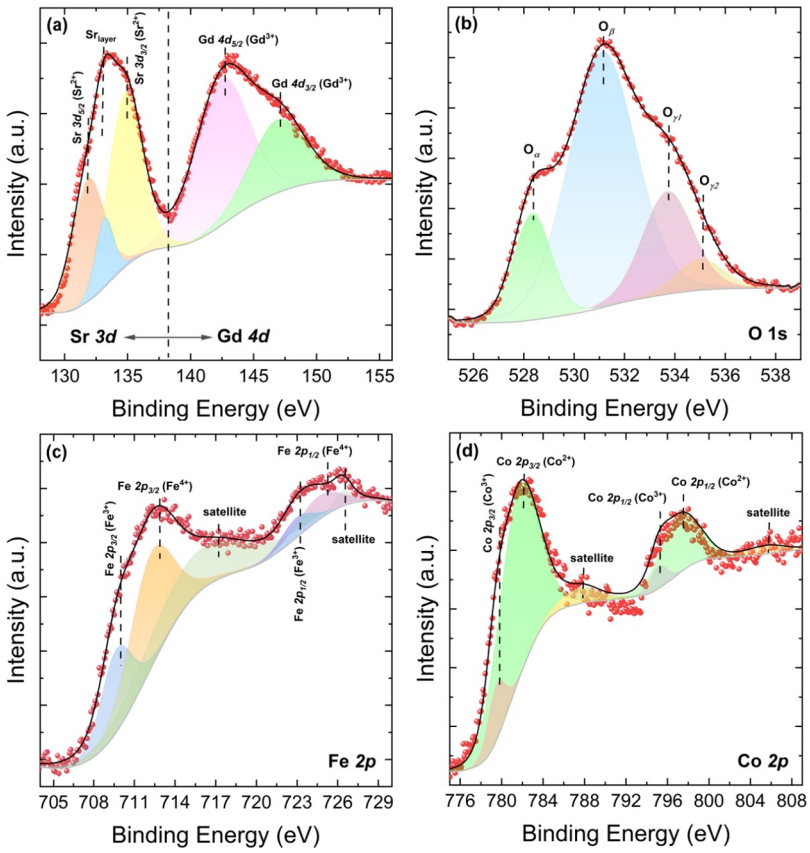

Figure 4. XPS spectra of Sr 3*d* and Gd 4*d* (a), O 1*s* (b), Fe 2*p* (c), and Co 2*p* (d) levels for the $GdSrCoFeO_6$ double perovskite.

such that d_s^2 is the intrinsic disorder and m is the atomic mass. Here, this atomic mass was averaged for each site of $GdSrCoFeO_6$. For instance, AA' = Gd,Sr $m_{Gd,Sr}$ = 122.435 u; BB' = Fe,Co $m_{Fe,Co}$ = 57.389 u; and oxygen O m_O = 15.999 u. Figure 2e represents the experimental U_{eq} values extracted from the Rietveld refinement together with the fitting provided by eq 2. The derived intrinsic disorder for all the sites are 7.6(8) × 10^{-3}, 2.4(2) × 10^{-3}, and 19.1 × 10^{-3} Å^2 for (Gd,Sr), (Fe,Co), and O, respectively. The Debye temperatures were obtained as follows: (Gd,Sr) (250(1) K), (Fe,Co) (472(5) K), and O (647(7) K). Those values can be used to estimate the bonding stiffness using the harmonic one-particle potential,[49] by applying the following expression:

$$K = \frac{mk_B^2\theta_D^2}{3\hbar^2} \quad (3)$$

where K is the force constant (in units of eV/Å^2), which showed values of 4.5, 7.6, and 4.0 eV/Å^2 for the (Gd,Sr), (Fe,Co), and O sites, respectively. Therefore, those values increase in the order $K_O < K_{(Gd,Sr)} \ll K_{(Fe,Co)}$, meaning that the distorted octahedral units of Co and Fe are more constrained to their motions (indeed, with d_s^2 = 2.4(2) × 10^{-3} Å^2). This conclusion essentially is because the bond (Fe,Co)−O is more covalent when compared to (Gd,Sr)−O, which has an intrinsic disorder of ∼3 times higher than that of the (Fe,Co) site.

STEM shows an atomic resolution image (annular dark field—ADF) of a crystallite of $GdSrFeCoO_6$ along the pseudocubic [100] zone axis, as shown in Figure 3. The yellow rectangle in panel (a) depicts the area where the EELS data are taken. Simultaneous ADF images and elemental maps based on the oxygen K, iron, cobalt, strontium $L_{2,3}$, and gadolinium $M_{4,5}$ edges (panel c) are shown in panel (b). These maps corroborate the finding of Gd and Sr sharing the AA'-site and Fe and Co sharing the BB'-site of the perovskite crystal structure. No site ordering can be detected in these elemental maps. Equally, no chemical inhomogeneity can be seen in the larger scale (up to 50 × 100 nm) EELS maps. This contrasts with the similar $SrGdMnTiO_6$ double perovskite, where noticeable spatial inhomogeneity of BB'-site atoms (Mn, Ti) was observed.[50]

The XPS technique was employed to determine the chemical states of Gd, Sr, Fe, Co, and O elements in the $GdSrCoFeO_6$ sample. Figure 4a shows that the core-level XPS spectrum for Gd 4*d* reveals two components at 142.5 eV (Gd 4$d_{5/2}$) and 146.9 eV (Gd 4$d_{3/2}$),[51,52] indicating that gadolinium exists in the form of Gd^{3+} (6.34 atom %) in $GdSrFeCoO_6$. The observed spectrum broad line shape is typical of rare earth elements with partially filled 4*f* shells due to an intrinsic line structure from the multiplet splitting.[53,54] The core-level XPS spectrum for Sr 3*d* (Figure 4a), which is at the lower binding energy side of the Gd 4*d* line, exhibits a spin-orbit doublet signal with binding energies of 134.8 eV (Sr 3$d_{3/2}$) and 131.9 eV (Sr 3$d_{5/2}$), which are assigned to Sr^{2+} ions at the AA'-site of the $GdSrFeCoO_6$ lattice (12.06 atom %).[55,56] Additionally, a component at 133.1 eV is also observed, which most likely indicates Sr^{2+} under-coordinated in the (Gd/Sr)−O-type termination layer on the surface of $GdSrFeCoO_6$ (Sr_{layer}: 1.21 atom %).[57−59]

The O 1*s* core-level spectrum was decomposed into three components, as shown in Figure 4b. The lowest binding energy peak at 528.3 eV (O_α) can be ascribed to oxygen atoms bonded to Gd/Sr and Fe/Co ions of the $GdSrFeCoO_6$ lattice

https://doi.org/10.1021/acs.chemmater.2c03574
Chem. Mater. 2023, 35, 2439−2455

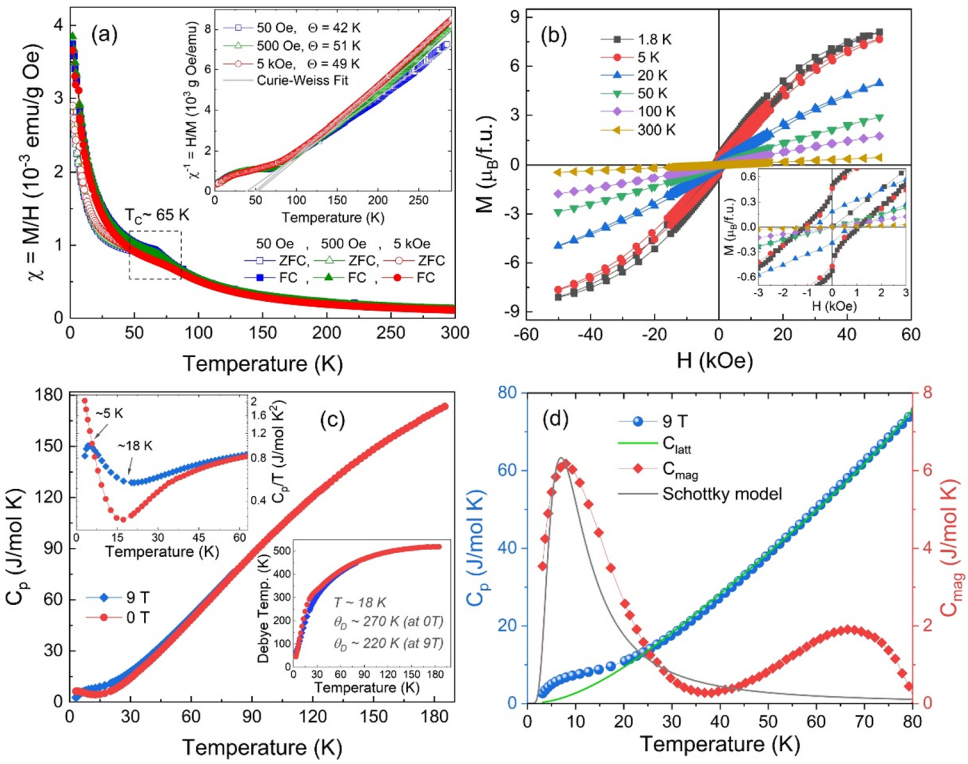

Figure 5. (a) Temperature-dependent magnetization of $GdSrCoFeO_6$ measured in an applied field of 100 Oe after cooling in zero applied field (ZFC) and in applied fields of 50 Oe, 500 Oe, and 5 kOe (FC). The inset shows the Curie−Weiss fitting in the paramagnetic region of the inverse susceptibility ($\chi^{-1} = H/M$) as a function of temperature. (b) Isothermal magnetization $M(H)$ curves at different temperatures of 1.8 up to 300 K under an external magnetic field H = 0 up to ±50 kOe. (c) Specific heat $C_p(T)$ curves at 0 and 9 T. (d) $C_{mag}(T)$ and $C_{latt}(T)$ curve at 9 T extracted through eqs 1 and 2. The gray curve shows a 2-level Schottky model single parameter fit to C_{mag} with $\Delta E/k_B$ = 18.5 K and double degenerate excited level.

(O_{latt}: 6.91 atom %).[60,61] The most intense peak at 531.1 eV (O_β: 29.72 atom %) corresponds to the contributions from Fe/Co cations located in the $[Co/Fe]O_6$ octahedra of the perovskite structure and Co/Fe−O surface species related to the termination layer.[62−64] Another two peaks at 533.7 ($O_{\gamma 1}$:) and 534.9 eV ($O_{\gamma 2}$) can be assigned to chemisorbed surface oxygen species of type O^-, O^{2-}, and OH^-.[56,65−67]

Figure 4c,d displays the core-level spectra for Fe 2*p* and Co 2*p*, respectively. In the deconvoluted high-resolution Fe 2*p* spectrum (Figure 4c), two distinct peaks at binding energies of 709.7 eV ($2p_{3/2}$) and 722.9 eV ($2p_{1/2}$), along with the satellite peak at 715.3 and 726.4 eV, are characteristic of Fe^{3+} (1.21 atom %) octahedral sites.[68,69] Additionally, peaks located at 712.2 ($2p_{3/2}$) and 724.6 eV ($2p_{1/2}$) confirm that Fe^{4+} (2.73 atom %) species is in a high spin state in the octahedral sites.[70,71] For the high-resolution Co 2*p* spectrum (Figure 4d), the first pair of peaks with lower binding energies centered at 779.5 and 795.2 eV can be ascribed to Co $2p_{3/2}$ and Co $2p_{1/2}$ of Co^{3+} (0.58 atom %), whereas another pair of peaks with a binding energy of 781.6 and 797.1 eV were attributed to the $2p_{3/2}$ and $2p_{1/2}$ of Co^{2+} (4.01 atom %),[65] respectively. The satellite peaks at 787.5 ($p_{3/2}$) and 805.5 ($p_{1/2}$) eV are consistent with the energy binding of high spin Co^{2+} species at the octahedral site.[72,73] Notably, spin-orbit component $2p_{3/2}$-$2p_{1/2}$ with a splitting value of 15.7 eV for Co^{3+} in the $GdSrFeCoO_6$ sample is about 0.85 eV larger than that reported for low spin state octahedral Co^{3+} ions (~14.85 eV).[74,75] However, our splitting value matches quite well to the value of 15.7 eV previously reported for conventional high-spin octahedral Co^{3+},[76−79] which is supported by our DFT results as discussed later.

3.2. Magnetic Properties. The temperature dependence of the susceptibility $\chi(T)$ of $GdSrCoFeO_6$ was determined experimentally with both field cooling (FC) and zero-field cooling (ZFC) in the temperature range of 1.8−300 K in different external fields of H = 50 Oe, 500 Oe, and 5 kOe, as illustrated in Figure 5a. $\chi(T)$ curves increase gradually with temperature decrease, which was also observed for other DP.[3,14,80,81] However, they exhibit a small pronounced peak around the Curie temperature $T_C \approx 65$ K. Noticeably, the peak at ~65 K is washed out by increasing the magnetic field up to 5 kOe, which can be associated with the tendency of complete spin orientation, i.e., a spin subset is still uncoupled align antiferromagnetically in the field direction and induces a magnetization decrease, also demonstrated by ac magnetic susceptibility frequency- and driving field-dependent (see Figure S4), which discard any SG-like nature in $GdSrCoFeO_6$ (more information in the SI). There is a small difference between ZFC/FC curves with the irreversibility temperature (T_{irr}) around T_C. This behavior is a typical characteristic of the SOPT from FM/FiM order to paramagnetic (PM) state.[5] The temperature of 65 K coincides well with that observed by temperature-dependent SXRD analysis at ~70 K (see Figure 2a−d), characterizing the magnetoelastic effect. In the low-temperature region (<70 K), the short- and long-range Co/Fe−O−Co/Fe and Gd−O−Gd interactions tend to be stronger due to the smaller ⟨(Co/Fe) − O⟩ and ⟨(Gd/Sr) − O⟩ average bond lengths in the structure (mainly in the *b*- and *c*-axis direction). As the temperature is increased (>70 K), the

https://doi.org/10.1021/acs.chemmater.2c03574
Chem. Mater. 2023, 35, 2439−2455

bond lengths considerably increase followed by the lattice thermal expansion (see the pronounced volume increase shown in Figure 2d), and evidently, the short- and long-range interactions weaken in the $GdSrCoFeO_6$ sample, resulting in the magnetic transition from FM/FiM order to PM state at $T_C \approx 65$ K.

The inverse susceptibility $\chi^{-1}(T)$ curves with external fields of 50 Oe, 500 Oe, and 5 kOe are illustrated in the inset of Figure 5a. Clearly, the curves follow the Curie−Weiss (C−W) law: $\chi = C/T - \Theta_{Weiss}$ at high temperature ($T > 150$ K), where Θ_{Weiss} denotes PM Curie temperature and C is the Curie constant.[18] However, below 100 K, the curves deviate entirely from the C−W law forming a paramagnetic-like tail with an intensity increase probably associated with the magnetic contribution provided by Gd^{3+} ions.[82] Their linear fittings yield positive Θ_{Weiss} values of 42 K (50 Oe), 51 K (500 Oe), and 49 K (5 kOe), which indicates the predominance FM/FiM interactions above T_C. We also observed that the frustration factor, defined as $f_{frus} = |\Theta_{Weiss}|/T_C$,[83] yields $f_{frus} = 0.65$, 0.78, and 0.75, respectively. Theses values are less than 1 and indicate that the system is not geometrically frustrated.[84−86] The observed paramagnetic moments (p_{eff}) are 11.1, 10.4, and 10.2 μ_B/f.u. for the three fields mentioned (50 Oe, 500 Oe, and 5 kOe). The total effective magnetic moment of $GdSrCoFeO_6$ has been calculated using the atomic compositions estimated from the XPS analysis, as follows: $\mu_{total} \approx [(\mu_{Gd^{3+}})^2 + 0.9(\mu_{Co^{2+}})^2 + 0.2(\mu_{Co^{3+}})^2 + 0.3(\mu_{Fe^{3+}})^2 + 0.6(\mu_{Fe^{4+}})^2]^{1/2}\mu_B$ resulting in $\mu_{total} \approx 9.1$ μ_B, with magnetic moments in the high-spin (HS) state for Gd^{3+} ($J = 7/2$, $g_J = 2$, $\mu = g_J J$ $\mu_B = 7.0$ μ_B), Co^{2+} ($S = 3/2$, $\mu = 3.87$ μ_B), Co^{3+} ($S = 2$, $\mu = 4.9$ μ_B), Fe^{3+} ($S = 5/2$, $\mu = 5.92$ μ_B), and Fe^{4+} ($S = 1$, $\mu = 2.82$ μ_B). This is in excellent agreement with the values determined from the C−W fit.

To further verify the magnetic ordering, isothermal magnetization $M(H)$ curves were measured at temperatures of 1.8, 5, 20, 50, 100, and 300 K under an external magnetic induction field H up to ±5 kOe, as shown in Figure 5b. Notably, the magnetic moment gradually decreases with increasing temperature from 1.8 up to 300 K. Moreover, magnetization at low temperatures (<20 K) tends to saturate up to 50 kOe, whereas at $T > 20$ K the curves are straight lines typical of a paramagnetic behavior. The observed unsaturability behavior in the $M(H)$ curves may be associated with the antisite disorder (ASD),[87,88] which favors the antiferromagnetic Fe−O−Fe and Co−O−Co superexchange interactions present in the B/B'-site octahedral chains and hinders the complete FM ordering of the $GdSrCoFeO_6$ sample up to the applied field of 50 kOe. Additionally, the observed magnetic moment value of 7.88 μ_B/f.u. from the $M(H)$ curve at 1.8 K (see Figure 5b) is in close agreement with only Gd^{3+} ions of 7.0 μ_B, indicating that the magnetization at low temperatures is mainly due to Gd^{3+} ions. Finally, the $\mu_{total} \approx 9.1$ μ_B value above T_C is larger than the effective moment of the Gd^{3+} (7.0 μ_B) ion in the PM state, confirming a contribution in the magnetism of $GdSrCoFeO_6$ from both Gd^{3+} ($J = 7/2$) and the $Co^{2+/3+}$ ($S = 3/2$, $S = 2$) and $Fe^{3+/4+}$ ($S = 5/2$, $S = 1$) ions.

In addition, we performed specific heat (C_p) measurements at 0 and 9 T as a function of temperature, as illustrated in Figure 5c. There is no clear transition in the $C_p(T)$ curve near T_C. However, the C_p/T vs T curves, shown in the top-left inset, reveal a broad downward hump at ∼18 K and another less wide upward at ∼5 K. The peak at ∼5 K (curve in 9 T) corresponds to the onset of AFM ordering of Gd^{3+} magnetic moments, whereas at ∼18 K is attributed to the Schottky contribution that arises from crystal field transitions related mostly to the f-electrons of Gd^{3+}. Similar behavior is commonly seen in other double perovskite compounds.[89−91] These anomalies are characteristic of disordered systems for which the competing magnetic interactions lead to short-range correlations.[20] The lower right inset in Figure 5c shows the θ_D as a function of temperature. As can be seen, the curve follows linearity up to $T \sim 18$ K, yielding $\theta_D \sim 270$ and 220 K for 0 and 9 T, respectively. It then shows a saturation trend up to 180 K, resulting in $\theta_D \sim 518$ K. Similar values were observed for other materials.[92] The high θ_D value will favor the magnetocaloric effect for the low lattice entropy during recuperative cycles.[93]

Figure 5d shows the $C_p(T)$ curve at 9 T from 2 up to 80 K (blue balls), where it is possible to clearly notice a hump-like feature extending from 2 up to 20 K. Generally, this is attributed to the magnetic contribution (C_{mag}) in $C_p(T)$ because the phononic and electronic contributions (in the case of insulators) are very weak at low temperature. Assuming that the electronic contribution is negligible at low temperatures, the method to separate the C_{mag} from $C_p(T)$ consists of subtracting the lattice contribution (C_{latt}) from the sample heat capacity C_p, following the relation 14:

$$C_{mag}(T, H) = C_{total}(T, H) - C_{latt}(T, H) \quad (4)$$

where the C_{latt} can be fitted through the C_p vs T data with the polynomial equation:

$$C_{latt} = aT^3 + bT^5 + cT^7 \quad (5)$$

where a, b, and c are constants to be fitted. The C_{latt} fitting by eq 2 is shown as a green line in Figure 5d. In the $C_{mag}(T)$ curve, two broad and well-defined peaks are centered on ∼10 and 70 K. The first one matches very well with the Schottky anomaly related mostly to Gd ions,[94] whereas the second can be associated with the magnetic transition of FM/FiM to PM order. Generally, the materials with atoms with f-electrons have this anomalous peak of low-temperature specific heat. The Schottky model explains this phenomenon through statistical physics by considering a few-level system with thermal occupation,[94,95] as $C_{Sch}(T) = \frac{R}{T^2}\left[\frac{\sum \nu_i \Delta_i^2 e^{-\Delta_i/T}}{\sum \nu_i e^{-\Delta_i/T}} - \left(\frac{\sum \nu_i \Delta_i e^{-\Delta_i/T}}{\sum \nu_i e^{-\Delta_i/T}}\right)^2\right]$. The model has energy gaps Δ_i (in K units) as free parameters, $\Delta_0 = 0$ corresponds to the ground level), while the number and degeneracy of levels ν_i are fixed, leaving only one fitting parameter for 2-level systems. At low temperatures, it is often sufficient to consider only the first excited level together with the ground level in 4f-electron systems. This results in a characteristic peak in the heat capacity for a two-level Schottky system. The degeneracies of the ground and excited levels in the Schottky model can be varied, and here they were chosen after analyzing several options in both fields. The gray curve in the Figure 5d shows a two-level Schottky model single parameter fit to $C_{mag}(T)$ curve with $\Delta E/k_B = 18.5$ K and double degenerate excited level obtained for the $GdSrCoFeO_6$ sample.

The critical behavior and MCE in $GdSrCoFeO_6$ were investigated through a series of isothermal magnetization $M(H)$ curves obtained with applied field H up to 70 kOe in the temperature range of 5−155 K and interval $\Delta T = 3$ K, as illustrated in Figure 6a. The magnetization shows a saturation

https://doi.org/10.1021/acs.chemmater.2c03574
Chem. Mater. 2023, 35, 2439−2455

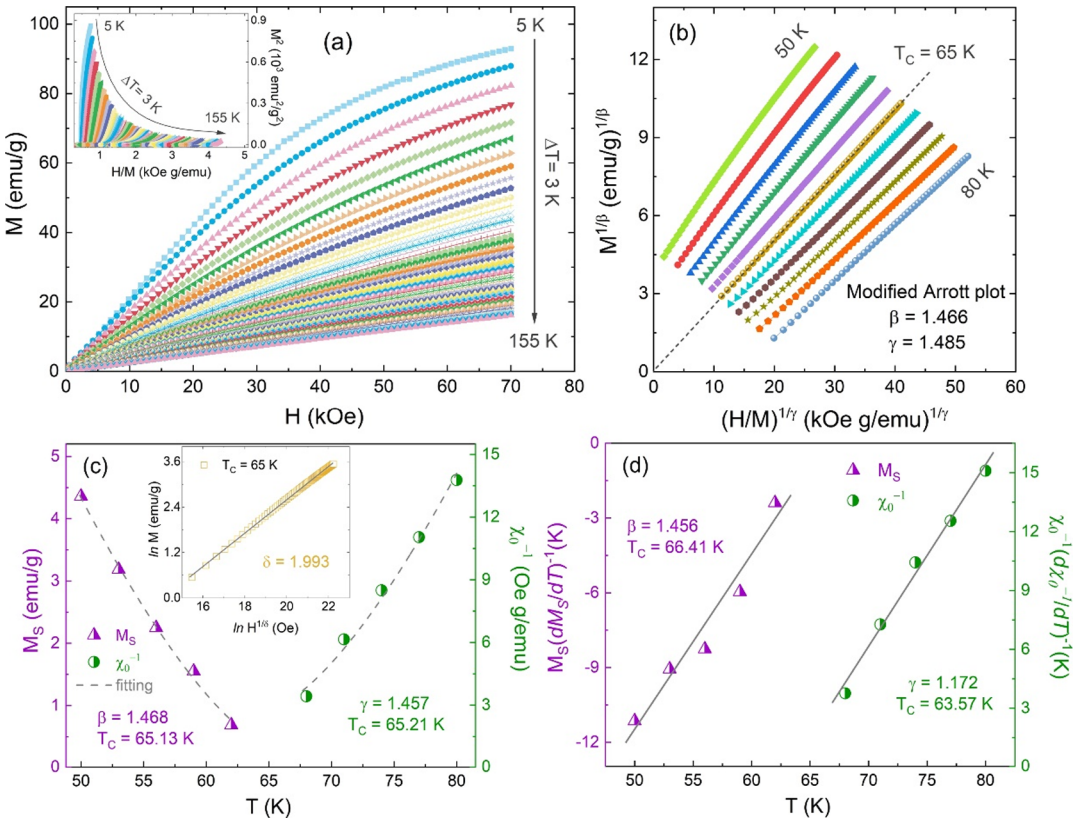

Figure 6. (a) Isotherms $M(H)$ measured at different temperatures from 5 up to 155 K, inset the Arrott plots (M^2 vs H/M). (b) Modified Arrott plot $(M)^{1/\beta}$ vs $(H/M)^{1/\gamma}$ constructed from $M(H)$ data with critical exponents $\beta = 1.466$ and $\gamma = 1.485$. (c) Spontaneous magnetization M_S and the temperature-dependent inverse initial magnetic susceptibility χ_0^{-1}, obtained from the high-field extrapolation of the modified Arrott plot. Inset shows an ln M vs ln $H^{1/\delta}$ plot from isotherm at $T_C = 65$ K. (d) Kouvel–Fisher plot for $M_S(T)$ and $\chi_0^{-1}(T)$ data.

tendency below T_C, whereas above T_C it increases almost linearly up to 70 kOe, characterizing the PM ground state. The MCE of the magnetic oxides has a strong relationship with the magnetic phase transition;[18] therefore, it is crucial to confirm the magnetic order type of $GdSrCoFeO_6$. Thus, $M(H)$ isotherms have been transformed into Arrott plots (H/M vs M^2) based on Banerjee criterion[96] and are shown in the inset of Figure 6a. The slopes of all curves are positive, which denotes a type of SOPT in $GdSrCoFeO_6$, and hence justifies a critical analysis.

To gain further insight into the FM/FiM to PM transition, we investigated in detail the critical behavior characterized by the critical exponents in $GdSrCoFeO_6$ by comparing several analysis methods. In the vicinity of SOPT, the diverging correlation length leads to the universal scaling laws for spontaneous magnetization (M_S), initial susceptibility (χ_0), and magnetization at T_C via a set of critical exponents β, γ, and δ.[20] Mathematically, the exponents from magnetization can be described as:[16,97]

$$M_S(0, \epsilon) \sim (-\epsilon)^{\beta}, \epsilon < 0, T < T_C \quad (6)$$

$$\chi_0^{-1}(0, \epsilon) \sim (\epsilon)^{\gamma}, \epsilon > 0, T > T_C \quad (7)$$

$$M(H, 0) \sim (H)^{1/\delta}, \epsilon = 0, T = T_C \quad (8)$$

where $\epsilon = (T - T_C)/T_C$ is the reduced temperature. The three exponents β, γ, and δ are coupled, and the Widom scaling relation predicts that $\delta = 1 + \gamma/\beta$.[98] According to the Arrott–Noakes equation of state, which describes $(H/M)^{1/\gamma} = a\epsilon + b(M)^{1/\beta}$ (a and b are constants), the modified Arrott plot (MAP) by $(M)^{1/\beta}$ vs $(H/M)^{1/\gamma}$ curves with proper β and γ values near T_C should produce a set of parallel straight lines, and the isotherm at T_C line should cross the origin of coordinates.[96,99] Indeed, Landau's mean-field theory with $\beta = 0.5$ and $\gamma = 1.0$ values predict that the M^2 vs H/M curves at various temperatures around T_C should be a series of parallel lines in the high-field region.[100] However, in our case, the M^2 vs H/M curves shown in the inset of Figure 6a do not exhibit this behavior, indicating that the mean-field model cannot characterize the critical trend of $GdSrCoFeO_6$. The 3D Ising model ($\beta = 0.325$, $\gamma = 1.24$), 3D Heisenberg model ($\beta = 0.365$, $\gamma = 1.386$), tricritical mean-field model ($\beta = 0.25$, $\gamma = 1.0$), and 3D XY model ($\beta = 0.345$, $\gamma = 1.316$)[40] were also tested, as exhibited in Figure S5, but neither describes well the critical behavior of $GdSrCoFeO_6$. Hence, a MAP should be employed to obtain the critical exponents.

First, by properly selecting the β and γ exponents, a set of parallel straight lines at high fields resulted in the MAP fitting (Figure 6b), yielding $\beta = 1.466$ and $\gamma = 1.485$. The obtained values follow a relationship $\beta \approx \gamma$, quite distinct from any conventional universality class. Second, separated by the critical isotherm in Figure 6b of 65 K, M_S and χ_0^{-1} have been extracted and plotted vs temperature (see Figure 6c) and analyzed with eqs 6 and 7, (gray dashed lines in Figure 6c) yielding $\beta = 1.468$ with $T_C = 65.13$ K and $\gamma = 1.457$ with $T_C = 65.21$ K. These values are very consistent with that achieved from the MAP plot. Using the Widom scaling relation $\delta = 1 + \gamma/\beta$,[20] we obtain $\delta = 1.993$. As shown in the inset of Figure 6c, the ln M vs ln $H^{1/\delta}$ curve for isotherm at $T_C = 65$ K obeys the

https://doi.org/10.1021/acs.chemmater.2c03574
Chem. Mater. 2023, 35, 2439−2455

linearity predicted by eq 5. Similarly, the β and γ values obtained by MAP fitting in Figure 6b reveal δ = 2.013.

Thirdly, these critical exponents can also be determined by the Kouvel–Fisher (KF) method,[101] described as follows:

$$\frac{M_S(T)}{dM_S(T)/dT} = \frac{T - T_C}{\beta} \tag{9}$$

$$\frac{\chi_0^{-1}(T)}{d\chi_0^{-1}(T)/dT} = \frac{T - T_C}{\gamma} \tag{10}$$

Notably, the temperature dependences of $M_S(T)[dM_S(T)/dT]^{-1}$ and $\chi_0^{-1}(T)[d\chi_0^{-1}(T)/dT]^{-1}$ yield straight lines with $1/\beta$ and $1/\gamma$ slopes, respectively, and the intercepts on the T axes are equal to T_C, yielding β = 1.456 with T_C = 66.41 K and γ = 1.172 with T_C = 63.57 K, respectively (Figure 6d). Evidently, the critical exponents from the KF method are consistent with those obtained by the MAP, which indicates their self-consistency. The critical exponents obtained from MAP and KF methods for $GdSrCoFeO_6$ are also shown in Table 2, compared with other DP compounds and theoretical model values.

Table 2. Comparison of Critical Exponents of $GdSrCoFeO_6$ Obtained from MAP and KF Methods with Other DP Compounds and Theoretical Models

composition	method	T_C (K)	β	γ	δ	reference
$GdSrCoFeO_6$	MAP	65	1.466	1.485	2.013	this work
	KF	64.99	1.456	1.172	1.805	
$NdSrCoFeO_6$	MAP	149	1.384	0.621	1.421	40
Gd_2CoMnO_6	MAP	123	1.18	0.65	1.55	20
Nd_2CoMnO_6	MAP	156	0.545	1.131	3.075	102
	KF	155.9	0.498	1.190	3.389	
Nd_2CrMnO_6	MAP	80	0.704	0.712	2.01	99
	KF	80.3	0.694	0.706	2.02	
mean field			0.5	1.0	3.0	100
tricritical mean field			0.25	1.0	5.0	100
3D Ising			0.325	1.24	4.82	100
3D Heisenberg			0.365	1.386	4.8	100
3D XY			0.345	1.316	4.81	100

In order to certify the reliability of the obtained critical exponents, the scaling hypothesis was analyzed by the magnetic equation of state in the asymptotic critical region, defined as:[20]

$$M(H, \epsilon) = |\epsilon|^{\beta} f_{\pm}\left(\frac{H}{|\epsilon|^{\beta\delta}}\right) \tag{11}$$

where $f_{\pm}$ are regular functions with f_+ for temperatures above T_C and f_- for temperatures below T_C. Using the β, δ, and T_C values obtained from MAP, we have represented the $M|\epsilon|^{-\beta}$ vs $H|\epsilon|^{-(\beta+\delta)}$ plot and the same plot in the log–log scale, as shown in Figure 7. The curves show a tendency collapsed into two different universal curves, one for $T > T_C$ (red) and another for $T < T_C$ (blue), which demonstrates that the critical exponents obtained here are reliable and in agreement with the scaling hypothesis.

Ultimately, the ΔS_M under various magnetic field changes (ΔH) was evaluated from the magnetization isotherms through Maxwell's thermodynamic relation expressed as:[4]

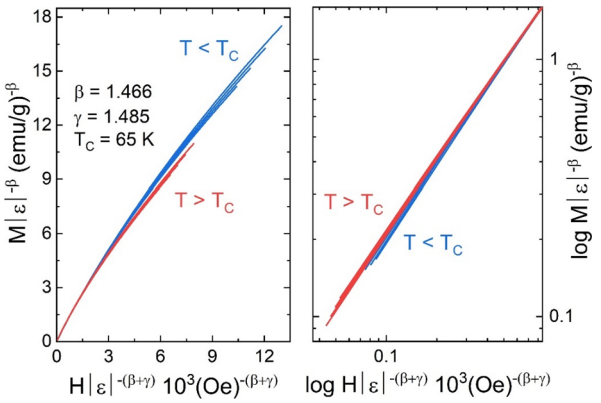

Figure 7. Scaling plot according to eq 11 for the curves at $T < T_C$ and $T > T_C$, and the same plot in the log–log scale.

$$|\Delta S_M(T, H)| = S_M(T, H) - S_M(T, 0) = \int_0^{H_{max}} \left(\frac{\partial M(T, H)}{\partial T}\right)_H dH \tag{12}$$

On the other hand, for discrete magnetization measurements, ΔS_M can be approximately calculated as:

$$\Delta S_M(T, H_0) = \sum_i \frac{M_{i+1} - M_i}{T_{i+1} - T_i} \Delta H_i \tag{13}$$

where M_i and M_{i+1} are the experimental data obtained at temperatures T_i and T_{i+1}, under a magnetic field H_i, respectively.[103,104] The results of $-\Delta S_M(T)$ curves for $GdSrCoFeO_6$ sample under several typical ΔH up to 7 T are illustrated in Figure 8a. All curves show positive values in the entire measured temperature range; they rise progressively with decreasing temperature and increase gradually with increasing ΔH, in agreement with the usual MCE behavior.

The pronounced peaks around 8 K present maximum entropy change $-\Delta S_M^{max}$ of 0.76, 2.91, 5.88, 8.90, 10.77, 12.12, and 12.98 J kg^{-1} K^{-1} for ΔH varying from 0–1 to 0–7 T, respectively. The $-\Delta S_M^{max}$ occurrence below the transition temperature can be associated with the partially induced moment on the Gd^{3+} rare earth ions.[22,89] This $-\Delta S_M^{max}$ observed value of 12.98 J kg^{-1} K^{-1} at 0–7 T is larger than that found in other Co/Fe-based DPs with 8.85 and 7.82 J kg^{-1} K^{-1} for Er_2FeCoO_6 and Gd_2FeCoO_6,[25] respectively. Moreover, our value is already 33.8% of commercialized gadolinium gallium garnet ($Gd_3Ga_5O_{12}$—GGO), which has long been developed and considered as a benchmark cryogenic magnetocaloric material with $-\Delta S_M^{max}$ = 38.4 J kg^{-1} K^{-1} under ΔH = 0–7 T around 2.0 K.[105,106] On the other hand, it is still far below the theoretical limit ($-\Delta S_{M-limit}$) which is usually estimated using the contribution of the uncoupled Gd^{3+} ions as $-\Delta S_{M-limit} = R \cdot \ln(2J + 1)$, where R represents the universal gas constant, and J accounts for the half-filled 4f orbital of Gd^{3+} ions with a high spin state of J = 7/2.[18] The $-\Delta S_{M-limit}$ calculated for $GdSrCoFeO_6$ was 75.89 J kg^{-1} K^{-1}. This discrepancy is probably related to the additional internal entropy loss from the phonon contribution as well as limitation of ΔH value in the measurements, which could lead the $M(H)$ curves to saturation, and consequently larger $-\Delta S_M^{max}$ would be achieved. Moreover, we observed that $-\Delta S_M^{max}$ follows a power-law as $-\Delta S_M^{max} \approx H^n$, as depicted in the inset of Figure 8a, with n = 0.75. Notably, n deviates from the mean-field ferromagnet

https://doi.org/10.1021/acs.chemmater.2c03574
Chem. Mater. 2023, 35, 2439–2455

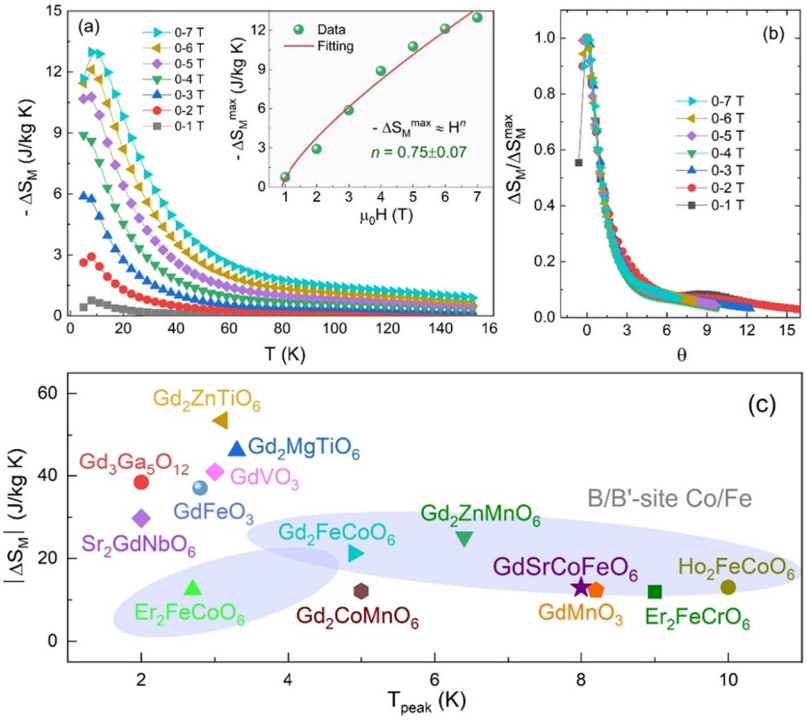

Figure 8. (a) Temperature dependence of the magnetic entropy change $-\Delta S_M(T)$ obtained from magnetization at magnetic fields ΔH varying from 0−1 to 0−7 T for $GdSrCoFeO_6$. (b) $\Delta S_M/\Delta S_M^{max}$ vs θ curves. (c) Comparison of $|\Delta S_M|$ value of $GdSrCoFeO_6$ with some recently reported cryogenic MCE oxide materials.

value $n = 2/3$,[97] which could be a consequence of the existence of local inhomogeneities or magnetic domains in the vicinity of the ordering temperature. Similar values have been reported for other DP.[107] The existence of FM/AFM magnetic competition, canted AFM, and long-range ordering of Gd^{3+} ions may be a possible reason for such a value of $-\Delta S_M^{max}$ in $GdSrCoFeO_6$.[108,109]

An interesting point regards the link between the magnetoelastic coupling and the MCE. The magnetoelastic coupling is a result of a tight interaction between the lattice and the magnetic interactions. It is manifested as a strongly anisotropic behavior of the unit-cell parameters upon cooling, in the sense that the crystal structure reacts against the establishment of the magnetic ordering, as a result of magnetic frustration. It is an intrinsic property of many magnetic materials where lattice strain induces changes in the internal magnetic fields. The MCE is also an intrinsic property of magnetic materials, due to the coupling of an external magnetic field with the magnetic sublattice. The magnetic moments are polarized by a magnetic field; upon demagnetization the magnetic entropy gain is compensated by a decrease of the vibrational entropy in adiabatic conditions, thus decreasing temperature. Hence, a coupling between magnetism and phonons is essential. A particularly intense MCE is observed in ferromagnets around their Curie temperatures; this effect is significantly increased when a ferromagnetic ordering is coupled to a structural transition e.g., in $Gd_5Si_2Ge_2$, where the MCE entropy change associated with its magnetostructural transition is doubled in comparison to the purely magnetic entropy change.[110] In the present case, we do not observe a phase transition, but a conspicuously strong lattice reorganization resulting from magnetostriction that reinforces the MCE in $GdSrCoFeO_6$. Therefore, the magnetic entropy change ΔS_M associated with the magnetoelastic coupling by the short-range magnetic interaction of ions in the system is intensified by the microscopic bond length changes and lattice reorganization upon cooling.

Additionally, to shed more light on the nature of the FM phase transition, we analyze the MCE through a normalizing universal curve, phenomenologically constructed by scaling all the $-\Delta S_M$ curves against the respective maximum $-\Delta S_M^{max}$ ($\Delta S_M/\Delta S_M^{max}$) and the reduced temperature $\theta_{\pm}$, as defined in the following equations:[100,111]

$$\theta_- = (T_{peak} - T)/(T_{r1} - T_{peak}),\ T < T_{peak} \quad (14)$$

$$\theta_+ = (T - T_{peak})/(T_{r2} - T_{peak}),\ T > T_{peak} \quad (15)$$

where T_{r1} and T_{r2} are the temperatures of two reference points determined by $\Delta S_M(T_{r1}, T_{r2}) = \frac{1}{2}\Delta S_M^{max}$. Applying this method, all the $\Delta S_M/\Delta S_M^{max}(\theta)$ curves for the magnetic fields 0 up to 7 T are rescaled and collapsed onto a single curve, as illustrated in Figure 8b. Such a trend resembles those of typical second-order phase transition materials,[18,111] confirming an FM-SOPT in $GdSrCoFeO_6$. The noncollapsed curves for $\theta < 0$ are attributed to uncertainties in the chosen reference temperature.

Figure 8c compares $|\Delta S_M|$ of $GdSrCoFeO_6$ with some recently reported cryogenic MCE materials[3,5,18,25,26,112−114] under ΔH = 5−7 T with working temperatures below 10 K. Indeed, the ΔS_M value of $GdSrCoFeO_6$ is far from the best values reported, so it should be improved to compete with other materials already well-considered for cryogenic magnetocaloric applications. However, their working temperature moves toward values suitable for application in hydrogen liquefaction.[1,115]

3.3. DFT Studies. To further investigate the electronic and magnetic characteristics of the $GdSrCoFeO_6$, DFT calculation was performed based on a GGA + U fully optimized cell with

https://doi.org/10.1021/acs.chemmater.2c03574
Chem. Mater. 2023, 35, 2439−2455

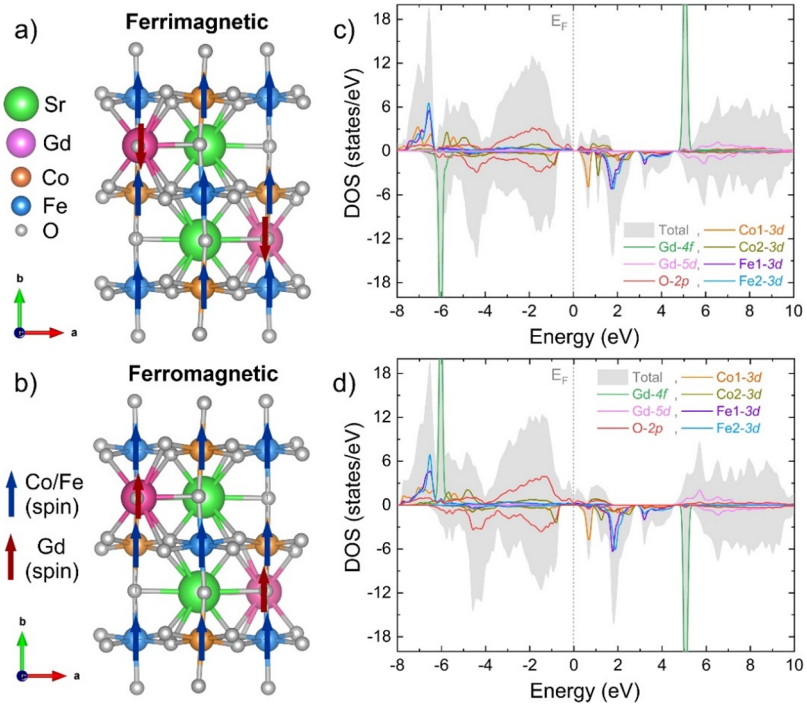

Figure 9. (a) Ferrimagnetic and (b) ferromagnetic alignment, and (c, d) their PBE + U total and partial spin-project states (TDOS and PDOS) calculated, respectively. The vertical dashed line indicates the Fermi energy level.

20 atoms, using structural parameters experimentally obtained in this work. The dual occupancy of the Gd/Sr and Co/Fe sites and their respective concentration are considered in a recent publication by our group,[40] where we demonstrated that the rock salt-like structure illustrated in Figure 9 is the closest to the description of a real system. Additionally, we computed different spin-magnetic configurations for the $GdSrCoFeO_6$ structure, where the minimum interaction energy was obtained for the FiM and FM ordering. These magnetic alignments used in the calculation are shown in Figure 9a,b, respectively. First, we performed the optimization of the lattice structural parameters. The results showed that a = 5.517 Å and c = 5.404 Å remain unchanged for both FiM and FM systems, but the b = 7.60 Å parameter for the FM cell is higher than the one found for the FiM cell (b = 7.487 Å), which characterizes the FM and FiM unit cells with optimized volumes of 227.793 and 223.237 $Å^3$, respectively, in agreement with the experimental results (see Table 1). This is because FM exchange interactions affect interatomic bonds, stretching the unit cell in the b-axis direction. Then, we proceed with the calculations of atomic positions and electronic structure. We found that the difference between the ground-state energies of the FiM and FM magnetic orders is only ∼0.05 eV, which confirms the experimental difficulty in affirming if the system is FiM or FM order. Furthermore, our calculations show calculated moments of 2.91 μ_B (Co1), 1.48 μ_B (Co2), 3.70 μ_B (Fe1), and 3.95 μ_B (Fe2) for the FiM alignment. The local magnetic moment on Co1 is higher than on the Co2 site; differently, the magnetic moment in Fe1 is smaller than in Fe2. This indicates that magnetic domains on Co1 and Fe2 octahedral sites favor longer-range magnetic interactions with their neighbors when compared to interactions created by Co2 and Fe1 ions. As a consequence of these differences in the intensity of the magnetic moments, short-range and long-range competitions arise in the $GdSrCoFeO_6$. The behavior for the FM system follows a similar trend, although a smaller difference is observed between the magnetic moments of Co1 (2.87 μ_B) and Co2 (1.62 μ_B), and between the Fe1 (3.83 μ_B) and Fe2 (3.87 μ_B). The magnetic moment at the Gd site is ∼7.0 μ_B for the two FiM and FM configurations.

Figure 9c,d illustrates the total and partial density of states (DOS) for the FiM and FM configurations, respectively. As can be seen, there are no significant differences between the FiM and FM electronic structures since their electron bands have almost the same shape, orbital character, and energy positions. However, the FiM ground-state DOS presents a semiconductor nature with a bang gap of ∼0.3 eV, while the FM shows a half-metallic behavior, specified by the valence spin-up band crossing the Fermi energy and by the gap of ∼1.2 eV in the spin-down band. The partial DOS at the valence band maximum is composed of a mixture of O-2p and Co-3d states, and the occupied Fe 3d states appear in the spin-up valence band channel in the low energy regions of −6.0 and −8.0 eV. The high exchange splitting of the Co1-3d and Fe2-3d spins evidences its higher magnetic moments, whereas the O 2p states exhibit more pronounced hybridization with Co 3d states than Fe 3d orbitals as a consequence of higher moments at the Fe sites favor longer-range interactions. The bottom of the conduction band is formed by an admixture of a spin-down peak of Co and a small band of O 2p states at the spin-up channel. Two almost overlapping spin-down bands of Fe 3d are positioned around 2 eV. The occupied electron states of Gd-4f appear as a highlighted peak near −6.0 eV in the spin-down and spin-up channels for FiM and FM, respectively. Its corresponding empty 4f states are positioned around 5.0 eV, while the unoccupied bands of the Gd 5d are located above 5.0 eV for the two FiM and FM cases. Additionally, our DFT results showed that the ground magnetic state of $GdSrCoFeO_6$ is FiM, with a thermally driven transition to FM alignment expected for low-temperature regions due to their closest

https://doi.org/10.1021/acs.chemmater.2c03574
Chem. Mater. 2023, 35, 2439−2455

ground-state energies. This very likely magnetic change is accompanied by an insulating-to-metal transition, which reveals the interesting fact that $GdSrCoFeO_6$ has related resonant magnetic (FM/FiM) and electronic (insulating/metal) properties. The magnetic properties are associated with the spin polarization of Gd and the short- and long-range competitions created by the different intensities of magnetic moments at the Co and Fe sites, while the electronic characteristics depend on crossings of spin states in the Co ions, facilitated by a crystal field splitting that allows electron transfers to the e.g. level, and by the oxygen-intermediated Co and Fe double exchange interaction.[40] Moreover, the Co average magnetic moment is slightly lower for the FiM than for the FM structure, indicating the electronic behavior of $GdSrCoFeO_6$ is sensitive to the Co magnetic moment intensity. The Gd rare earth ion also influences the related resonant magnetic and electronic process since the difference between the calculated FiM and FM magnetic orders is the spin projection on the Gd atoms. Despite their highly localized character, the FM DOS shows that the Gd-4*f* states slightly hybridize with the Co2-3*d* orbitals nearing −6.0 eV, causing the Co2 magnetic moment to increase. Consequently, the degree of hybridization of Co2 with its neighboring oxygens decreases, which is observed with the narrowing of the spin-down energy band around −1.0 eV. At the same time, causing a flattening of the Co1-3*d* spin-up band around −7.0 eV, and a consequent decrease in its spin polarization. Finally, our first-principles calculations prediction matches well with experimental results and sheds light on the magnetic and electronic properties of $GdSrCoFeO_6$. It reveals that the observed low-temperature FM/FiM and insulating/metal transitions are related to a combined effect of Co and Fe short- and long-range competitions, crossings of spin state at Co ions, and the hybridization degree between Gd-4*f* and Co-3*d* states.

4. CONCLUSIONS

In summary, a systematic study of the structural, magnetic, and magnetocaloric properties of the $GdSrCoFeO_6$ double perovskite has been realized. Structural analysis reveals that this sample crystallizes into a disordered orthorhombic (*Pnma*) structure at room temperature, in which Gd^{3+}/Sr^{2+} and $Co^{2+/3+}/Fe^{3+/4+}$ ions are randomly distributed at the *AA′* and *BB′* sites, respectively. The observed magnetic order transition from FM/FiM to PM at $T_C \approx 65$ K correlated with the magnetoelastic coupling revealed by SXRD analysis through the temperature-dependent lattice parameters. The first-principles calculations prediction matched well with experimental results and revealed that the observed low-temperature FM/FiM and insulating/metal transitions are related to a combined effect of Co and Fe short- and long-range competitions, crossings of spin state at Co ions, and the hybridization degree between Gd-4*f* and Co-3*d* states. Additionally, the nature of the magnetic transition was established using the critical exponent analysis and scale hypothesis, which is quite distinct from any conventional universality class. The Schottky anomaly related mostly to Gd ions at low temperature (∼8 K) revealed by specific heat analysis coincides well with the pronounced magnetocaloric effect of $-\Delta S_M^{max} \approx 13$ J kg^{-1} K^{-1} under a field of 0−7 T, that is 33.8% of commercialized gadolinium gallium garnet ($Gd_3Ga_5O_{12}$—GGO). Moreover, it has been observed that $-\Delta S_M^{max}$ follows a power-law behavior as $-\Delta S_M^{max} \approx H^n$ with n = 0.75, which demonstrates the existence of inhomogeneity local magnetic domains. Therefore, DFT findings together with the Gd-related MCE behavior make $GdSrCoFeO_6$ a remarkable candidate for cryogenic and technological applications.

■ ASSOCIATED CONTENT

Supporting Information

The Supporting Information is available free of charge at https://pubs.acs.org/doi/10.1021/acs.chemmater.2c03574.

Figure S1: Room-temperature XRD pattern and Rietveld refinement of $GdSrCoFeO_6$ double perovskite; Figure S2: SXRD Rietveld refinement test at room temperature in the monoclinic structure ($P2_1/n$); Figure S3: SXRD Rietveld refinement plot at the temperature of 6 K; Figure S4: Temperature dependence of the real χ_{ac}' part of the ac magnetic susceptibility measured at different frequencies of f = 100 Hz to 10 kHz, and Figure S5: Modified Arrott isotherms plotted as $M^{1/\beta}$ vs $(H/M)^{1/\gamma}$ (PDF)

■ AUTHOR INFORMATION

Corresponding Author

José Antonio Alonso − *Instituto de Ciencia de Materiales de Madrid (ICMM), CSIC, E-28049 Madrid, Spain;* orcid.org/0000-0001-5329-1225; Email: ja.alonso@icmm.csic.es

Authors

Romualdo S. Silva, Jr − *Instituto de Ciencia de Materiales de Madrid (ICMM), CSIC, E-28049 Madrid, Spain; Department of Physics, Federal University of Sergipe, 49100-000 São Cristóvão, SE, Brazil;* orcid.org/0000-0002-6749-5293

Javier Gainza − *Instituto de Ciencia de Materiales de Madrid (ICMM), CSIC, E-28049 Madrid, Spain;* orcid.org/0000-0002-1999-3116

Cledson dos Santos − *Department of Physics, Federal University of Sergipe, 49100-000 São Cristóvão, SE, Brazil*

João Elias F. S. Rodrigues − *Instituto de Ciencia de Materiales de Madrid (ICMM), CSIC, E-28049 Madrid, Spain; European Synchrotron Radiation Facility (ESRF), 38000 Grenoble, France;* orcid.org/0000-0002-9220-5809

Catherine Dejoie − *European Synchrotron Radiation Facility (ESRF), 38000 Grenoble, France;* orcid.org/0000-0003-3313-3515

Yves Huttel − *Instituto de Ciencia de Materiales de Madrid (ICMM), CSIC, E-28049 Madrid, Spain;* orcid.org/0000-0002-3683-9890

Nevenko Biskup − *Instituto Pluridisciplinar, Universidad Complutense de Madrid, E-28040 Madrid, Spain; Departamento Física de Materiales, Universidad Complutense de Madrid, E-28040 Madrid, Spain*

Norbert M. Nemes − *Instituto de Ciencia de Materiales de Madrid (ICMM), CSIC, E-28049 Madrid, Spain; Departamento Física de Materiales, Universidad Complutense de Madrid, E-28040 Madrid, Spain*

José Luis Martínez − *Instituto de Ciencia de Materiales de Madrid (ICMM), CSIC, E-28049 Madrid, Spain*

Nilson S. Ferreira − *Department of Physics, Federal University of Sergipe, 49100-000 São Cristóvão, SE, Brazil;* orcid.org/0000-0002-8421-2558

Complete contact information is available at:

https://pubs.acs.org/10.1021/acs.chemmater.2c03574

Notes

The authors declare no competing financial interest.

■ ACKNOWLEDGMENTS

This research was supported by the Coordenação de Aperfeiçoamento de Pessoal de Nível Superior-CAPES (Finance Code-001), Conselho Nacional de Desenvolvimento Científico e Tecnológico-CNPq (grant no. 309054/2019-2), and Spanish Ministry for Science and Innovation (MCIN/AEI/10.13039/501100011033) with grant nos.: PID2021-122477OB-I00, TED2021-129254B-C22, and PID2021-122980OB-C51. J.G. thanks MICINN for granting the contract PRE2018-083398. The authors wish to express their gratitude to the ESRF technical staff for making the facilities available for the synchrotron powder diffraction experiment (proposal HC-4990). Our thanks are also extended to the WIEN2k team of the Institute of Materials Chemistry (TU Vienna).

■ REFERENCES

(1) Tang, X.; Sepehri-Amin, H.; Terada, N.; Martin-Cid, A.; Kurniawan, I.; Kobayashi, S.; Kotani, Y.; Takeya, H.; Lai, J.; Matsushita, Y.; Ohkubo, T.; Miura, Y.; Nakamura, T.; Hono, K. Magnetic Refrigeration Material Operating at a Full Temperature Range Required for Hydrogen Liquefaction. *Nat. Commun.* **2022**, *13*, 1817.

(2) Gschneidner, A.; Pecharsky, V. K.; Tsokol, A. O. Recent Developments in Magnetocaloric Materials. *Rep. Prog. Phys.* **2005**, *68*, 1479.

(3) Yang, Z.; Ge, J. Y.; Ruan, S.; Cui, H.; Zeng, Y. J. Cryogenic Magnetocaloric Effect in Distorted Double-Perovskite Gd2ZnTiO6. *J. Mater. Chem. C* **2021**, *9*, 6754.

(4) Franco, V.; Blázquez, J. S.; Ipus, J. J.; Law, J. Y.; Moreno-Ramírez, L. M.; Conde, A. Magnetocaloric Effect: From Materials Research to Refrigeration Devices. *Prog. Mater. Sci.* **2018**, *93*, 112−232.

(5) Xu, P.; Ma, Z.; Wang, P.; Wang, H.; Li, L. Excellent Cryogenic Magnetocaloric Performances in Ferromagnetic Sr2GdNbO6 Double Perovskite Compound. *Mater. Today Phys.* **2021**, *20*, No. 100470.

(6) Franco, V.; Law, J. Y.; Conde, A.; Brabander, V.; Karpenkov, D. Y.; Radulov, I.; Skokov, K.; Gutfleisch, O. Predicting the Tricritical Point Composition of a Series of LaFeSi Magnetocaloric Alloys via Universal Scaling. *J. Phys. D Appl. Phys.* **2017**, *50*, 414004.

(7) Law, J. Y.; Franco, V.; Moreno-Ramírez, L. M.; Conde, A.; Karpenkov, D. Y.; Radulov, I.; Skokov, K. P.; Gutfleisch, O. A Quantitative Criterion for Determining the Order of Magnetic Phase Transitions Using the Magnetocaloric Effect. *Nat. Commun.* **2018**, *9*, 2680.

(8) Provenzano, V.; Shapiro, A. J.; Shull, R. D. Reduction of Hysteresis Losses in the Magnetic Refrigerant Gd 5Ge2Si2 by the Addition of Iron. *Nature* **2004**, *429*, 853.

(9) Li, L.; Yan, M. Recent Progresses in Exploring the Rare Earth Based Intermetallic Compounds for Cryogenic Magnetic Refrigeration. *J. Alloys Compd.* **2020**, *68*, No. 153810.

(10) Terada, N.; Mamiya, H. High-Efficiency Magnetic Refrigeration Using Holmium. *Nat. Commun.* **2021**, *12*, 1212.

(11) Palacios, E.; Tomasi, C.; Sáez-Puche, R.; Dos Santos-García, A. J.; Fernández-Martínez, F.; Burriel, R. Effect of Gd Polarization on the Large Magnetocaloric Effect of GdCrO4 in a Broad Temperature Range. *Phys. Rev. B* **2016**, *93*, No. 064420.

(12) Lyubina, J. Magnetocaloric Materials for Energy Efficient Cooling. *J. Phys. D: Appl. Phys.* **2017**, *50*, No. 053002.

(13) Yuan, Y.; Wu, Y.; Tong, X.; Zhang, H.; Wang, H.; Liu, X. J.; Ma, L.; Suo, H. L.; Lu, Z. P. Rare-Earth High-Entropy Alloys with Giant Magnetocaloric Effect. *Acta Mater.* **2017**, *125*, 481.

(14) Koskelo, E. C.; Liu, C.; Mukherjee, P.; Kelly, N. D.; Dutton, S. E. Free-Spin Dominated Magnetocaloric Effect in Dense Gd 3+ Double Perovskites. *Chem. Mater.* **2022**, *34*, 3440.

(15) Zeleňáková, A.; Hrubovčák, P.; Berkutova, A.; Šofranko, O.; Kučerka, N.; Ivankov, O.; Kuklin, A.; Girman, V.; Zeleňák, V. Gadolinium-Oxide Nanoparticles for Cryogenic Magnetocaloric Applications. *Sci. Rep.* **2022**, *12*, 2282.

(16) Falsaperna, M.; Saines, P. J. Development of Magnetocaloric Coordination Polymers for Low Temperature Cooling. *Dalton Trans.* **2022**, *51*, 3394.

(17) Peña, M. A.; Fierro, J. L. G. Chemical Structures and Performance of Perovskite Oxides. *Chem. Rev.* **2001**, *101*, 1981−2018.

(18) Zhang, Y.; Tian, Y.; Zhang, Z.; Jia, Y.; Zhang, B.; Jiang, M.; Wang, J.; Ren, Z. Magnetic Properties and Giant Cryogenic Magnetocaloric Effect in B-Site Ordered Antiferromagnetic Gd2MgTiO6 Double Perovskite Oxide. *Acta Mater.* **2022**, *226*, No. 117669.

(19) Sahoo, R. C.; Takeuchi, Y.; Ohtomo, A.; Hossain, Z. Exchange Bias and Spin Glass States Driven by Antisite Disorder in the Double Perovskite Compound LaSrCoFeO6. *Phys. Rev. B* **2019**, *100*, No. 214436.

(20) Das, M.; Sarkar, P.; Mandal, P. Non-Griffiths-like Cluster Formation in the Double-Perovskite Gd2CoMnO6: Evidence from Critical Behavior. *Phys. Rev. B* **2020**, *101*, No. 144433.

(21) Pal, A.; Singh, P.; Gangwar, V. K.; Ghosh, S.; Prakash, P.; Saha, S. K.; Das, A.; Kumar, M.; Ghosh, A. K.; Chatterjee, S. B-Site Disorder Driven Multiple-Magnetic Phases: Griffiths Phase, Re-Entrant Cluster Glass, and Exchange Bias in Pr2CoFeO6. *Appl. Phys. Lett.* **2019**, *114*, 252403.

(22) Mazumdar, D.; das, I. Structural, Magnetic, and Magnetocaloric Properties of the Multiferroic Host Double Perovskite Compound Pr2FeCrO6. *Phys. Chem. Chem. Phys.* **2021**, *23*, 5596.

(23) Sun, C.; Alonso, J. A.; Bian, J. Recent Advances in Perovskite-Type Oxides for Energy Conversion and Storage Applications. *Adv. Energy Mater.* **2021**, *11*, No. 2000459.

(24) Saha-Dasgupta, T. Ferroic Properties in Bi-Component Perovskites: Artificial Superlattices and Naturally Forming Compounds. *J. Phys. Condensed Matter.* **2014**, *26*, No. 193201.

(25) Dong, Z.; Wang, Z.; Yin, S. Structural, Magnetic and Magnetocaloric Properties in Perovskite RE2FeCoO6 (RE = Er and Gd) Compounds. *Ceram. Int.* **2020**, *46*, 26632.

(26) Das, M.; Mandal, P. Nonlinear Magnetodielectric and Magnetocaloric Properties of Double Perovskite Ho2FeCoO6. *Phys. B* **2019**, *571*, 32.

(27) Li, L.; Yan, M. Recent Progress in the Development of RE2TMTM'O6 Double Perovskite Oxides for Cryogenic Magnetic Refrigeration. *J. Mater. Sci. Technol.* **2023**, *136*, 1−12.

(28) Li, C.; Zheng, S.; Qiu, Y.; Lei, Q.; Wang, C.; Lu, Y.; Yang, Y.; Yan, H.; Luo, Y. Effect of Ti Substitution on Structural, Magnetic and Magnetocaloric Properties in Double Perovskites Gd 2 NiMn 1- x Ti x O 6 (0 ≤ x ≤ 1). 2022, *49*, 6891−6898, DOI: 10.1016/j.ceramint.2022.10.091.

(29) Zhitomirsky, M. E. Enhanced Magnetocaloric Effect in Frustrated Magnets. *Phys. Rev. B Condens. Matter Mater. Phys.* **2003**, *67*, No. 104421.

(30) Chogondahalli Muniraju, N. K.; Baral, R.; Tian, Y.; Li, R.; Poudel, N.; Gofryk, K.; Barišić, N.; Kiefer, B.; Ross, J. H.; Nair, H. S. Magnetocaloric Effect in a Frustrated Gd-Garnet with No Long-Range Magnetic Order. *Inorg. Chem.* **2020**, *59*, 15144.

(31) Fitch, A.; Dejoie, C. Combining a Multi-Analyzer Stage with a Two-Dimensional Detector for High-Resolution Powder X-Ray Diffraction: Correcting the Angular Scale. *J. Appl. Crystallogr.* **2021**, *54*, 1088−1099.

(32) Rodríguez-Carvajal, J. Recent Advances in Magnetic Structure Determination by Neutron Powder Diffraction. *Phys. B Phys. Condens. Matter* **1993**, *192*, 55−69.

(33) Nevshupa, R.; Martínez, L.; Álvarez, L.; López, M. F.; Huttel, Y.; Méndez, J.; Román, E. Influence of Thermal Ageing on Surface

Degradation of Ethylene-Propylene-Diene Elastomer. *J. Appl. Polym. Sci.* **2011**, *119*, 242.
(34) Hohenberg, P.; Kohn, W. Inhomogeneous Electron Gas. *Phys. Rev.* **1964**, *136*, B864.
(35) Kohn, W.; Sham, L. J. Self-Consistent Equations Including Exchange and Correlation Effects. *Phys. Rev.* **1965**, *140*, A1133.
(36) Blaha, P.; Schwarz, K.; Madsen, G.; Kvasnicka, D.; Luitz, J. *WIEN2k: An Augmented Plan Wave Plus Local Orbitals Program for Calculating Crystal Properties*; Technische Universität Wien: Wien, 2014; Vol. *28*.
(37) Andersen, O. K. Linear Methods in Band Theory. *Phys. Rev. B* **1975**, *12*, 3060.
(38) Perdew, J. P.; Ruzsinszky, A.; Csonka, G. I.; Vydrov, O. A.; Scuseria, G. E.; Constantin, L. A.; Zhou, X.; Burke, K. Restoring the Density-Gradient Expansion for Exchange in Solids and Surfaces. *Phys. Rev. Lett.* **2008**, *100*, No. 136406.
(39) Anisimov, V. I.; Poteryaev, A. I.; Korotin, M. A.; Anokhin, A. O.; Kotliar, G. First-Principles Calculations of the Electronic Structure and Spectra of Strongly Correlated Systems: Dynamical Mean-Field Theory. *J. Phys. Condens. Matter* **1997**, *9*, 7359.
(40) Silva, R. S.; Santos, C.; Escote, M. T.; Costa, B. F. O.; Moreno, N. O.; Paz, S. P. A.; Angélica, R. S.; Ferreira, N. S. Griffiths-like Phase, Large Magnetocaloric Effect, and Unconventional Critical Behavior in the NdSrCoFe O6 Disordered Double Perovskite. *Phys. Rev. B* **2022**, *106*, No. 134439.
(41) Li, Y.; Cheng, J.; Song, J.; Alonso, J. A.; Fernández-Díaz, M. T.; Goodenough, J. B. Characterization of the Double Perovskite Ba 2Bi XSc 0.2Co 1.8- XO 6-δ (x = 0.1, 0.2). *Chem. Mater.* **2012**, *24*, 4114.
(42) Momma, K.; Izumi, F. VESTA: A Three-Dimensional Visualization System for Electronic and Structural Analysis. *J. Appl. Crystallogr.* **2008**, *41*, 653.
(43) Nasir, M.; Khan, M.; Agbo, S. A.; Bhatt, S.; Kumar, S.; Sen, S. Evidence of Cluster-Glass and Griffiths-like Phases in Partially Ordered La2FeMnO6double Perovskite. *J. Phys. D Appl. Phys.* **2020**, *53*, 375003.
(44) Aswathi, K.; Palakkal, J. P.; Lekshmi, P. N.; Varma, M. R. A Griffiths-like Phase and Variable Range Hopping of Polarons in Orthorhombic Perovskite Pr2CrMnO6. *New J. Chem.* **2019**, *43*, 17351.
(45) Vočadlo, L.; Knight, K. S.; Price, G. D.; Wood, I. G. Thermal Expansion and Crystal Structure of FeSi between 4 and 1173 K Determined by Time-of-Flight Neutron Powder Diffraction. *Phys. Chem. Miner.* **2002**, *29*, 132−139.
(46) Nakatsuka, A.; Kuribayashi, S.; Nakayama, N.; Fukui, H.; Arima, H.; Yoneda, A.; Yoshiasa, A. Temperature Dependence of Crystal Structure of CaGeO 3 High-Pressure Perovskite Phase and Experimental Determination of Its Debye Temperatures Studied by Low- and High-Temperature Single-Crystal X-Ray Diffraction. *Am. Mineral.* **2015**, *100*, 1190−1202.
(47) Knight, K. S. Low-Temperature Thermophysical and Crystallographic Properties of BaZrO3 Perovskite. *J. Mater. Sci.* **2020**, *55*, 6417−6428.
(48) Nakatsuka, A.; Yoshiasa, A.; Fujiwara, K.; Ohtaka, O. Variable-Temperature Single-Crystal X-Ray Diffraction Study of SrGeO3 High-Pressure Perovskite Phase. *J. Mineral. Petrol. Sci.* **2018**, *113*, 280−285.
(49) Rodrigues, J. E. F. S.; Escanhoela, C. A.; Fragoso, B.; Sombrio, G.; Ferrer, M. M.; Álvarez-Galván, C.; Fernández-Díaz, M. T.; Souza, J. A.; Ferreira, F. F.; Pecharromán, C.; Alonso, J. A. Experimental and Theoretical Investigations on the Structural, Electronic, and Vibrational Properties of Cs 2 AgSbCl 6 Double Perovskite. *Ind. Eng. Chem. Res.* **2021**, *60*, 18918.
(50) Biškup, N.; Álvarez-Serrano, I.; Veiga, M.; Rivera-Calzada, A.; Garcia-Hernandez, M.; Pennycook, S. J.; Varela, M. Mapping Chemical Disorder and Ferroelectric Distortions in the Double Perovskite Compound Sr2-XGdxMnTiO6 by Atomic Resolution Electron Microscopy and Spectroscopy. In. *Microsc. Microanal.* **2014**, *20*, 731.
(51) Cummins, T. R.; Egdell, R. G. Electron Energy Levels in Nd2-XCexCuO4: A Study by Valence- and Core-Level Photoemission Spectroscopy. *Phys. Rev. B* **1993**, *48*, 6556.
(52) Raaen, S.; Parks, R. D. Shakedown Satellites near LIII Absorption Edges. *J. Magn. Magn. Mater.* **1985**, *47−48*, 200−202.
(53) Wandelt, K.; Brundle, C. R. The Interaction of Oxygen with Gadolinium: UPS and XPS Studies. *Surf. Sci.* **1985**, *157*, 162.
(54) Kowalczyk, S. P.; Edelstein, N.; McFeely, F. R.; Ley, L.; Shirley, D. A. X-Ray Photoemission Spectra of the 4d Levels in Rare-Earth Metals. *Chem. Phys. Lett.* **1974**, *29*, 491.
(55) Liu, B.; Zhang, Y.; Tang, L. X-Ray Photoelectron Spectroscopic Studies of Ba0.5Sr0.5Co0.8Fe0.2O3-δ Cathode for Solid Oxide Fuel Cells. *Int. J. Hydrogen Energy* **2009**, *34*, 435.
(56) Kuyyalil, J.; Newby, D.; Laverock, J.; Yu, Y.; Cetin, D.; Basu, S. N.; Ludwig, K.; Smith, K. E. Vacancy Assisted SrO Formation on La0.8Sr0.2Co0.2Fe0.8O3- δ Surfaces - A Synchrotron Photoemission Study. *Surf. Sci.* **2015**, *642*, 33.
(57) Santiso, J.; Fraxedas, J.; Figueras, A. Study of Sr2FeMoO6 PLD Films by In Situ XPS. *Surf. Sci. Spectra* **2002**, *9*, 39.
(58) Santiso, J.; Fraxedas, J.; Balcells, L.; Fontcuberta, J.; Figueras, A. In Situ Characterisation of Sr2FeMoO6films Prepared by Pulsed Laser Deposition. *J. Phys. IV* **2001**, *11*, Pr11-307.
(59) Silva, R. S.; Ferreira, N. S.; Maia da Costa, M.; Barrozo, P. Toward the Stabilization of Perovskite Phase at Low Temperature and Decrease of the Magnetic Ordering by Sr2+-Doping in LaCrO3. *Chem. Phys. Lett.* **2022**, *787*, No. 139278.
(60) Merino, N. A.; Barbero, B. P.; Eloy, P.; Cadús, L. E. La 1-x Ca x CoO 3 Perovskite-Type Oxides: Identification of the Surface Oxygen Species by XPS. *Appl. Surf. Sci.* **2006**, *253*, 1489.
(61) Opitz, A. K.; Rameshan, C.; Kubicek, M.; Rupp, G. M.; Nenning, A.; Götsch, T.; Blume, R.; Hävecker, M.; Knop-Gericke, A.; Rupprechter, G.; Klötzer, B.; Fleig, J. The Chemical Evolution of the La0.6Sr0.4CoO3−Δ Surface Under SOFC Operating Conditions and Its Implications for Electrochemical Oxygen Exchange Activity. *Top. Catal.* **2018**, *61*, 2129.
(62) Van Der Heide, P. A. W. Systematic X-Ray Photoelectron Spectroscopic Study of La1-XSrx-Based Perovskite-Type Oxides. *Surf. Interface Anal.* **2002**, *33*, 414.
(63) Yan, A.; Maragou, V.; Arico, A.; Cheng, M.; Tsiakaras, P. Investigation of a Ba0.5Sr0.5Co0.8Fe0.2O3-δ Based Cathode SOFC. II. The Effect of CO2 on the Chemical Stability. *Appl. Catal. B Environ.* **2007**, *76*, 320−327.
(64) Konysheva, E. Y.; Kuznetsov, M. V. Fluctuation of Surface Composition and Chemical States at the Hetero-Interface in Composites Comprised of a Phase with Perovskite Structure and a Phase Related to the Ruddlesden-Popper Family of Compounds. *RSC Adv.* **2013**, *3*, 14114.
(65) Abdel-Khalek, E. K.; Motawea, M. A.; Aboelnasr, M. A.; El-Bahnasawy, H. H. Study the Oxygen Vacancies and Fe Oxidation States in CaFeO3-δ Perovskite Nanomaterial. *Phys. B* **2022**, *624*, No. 413415.
(66) Ha, M. N.; Lu, G.; Liu, Z.; Wang, L.; Zhao, Z. 3DOM-LaSrCoFeO6-: δ as a Highly Active Catalyst for the Thermal and Photothermal Reduction of CO2 with H2O to CH4. *J. Mater. Chem. A* **2016**, *4*, 13155.
(67) Chang, H.; Bjørgum, E.; Mihai, O.; Yang, J.; Lein, H. L.; Grande, T.; Raaen, S.; Zhu, Y. A.; Holmen, A.; Chen, D. Effects of Oxygen Mobility in La-Fe-Based Perovskites on the Catalytic Activity and Selectivity of Methane Oxidation. *ACS Catal.* **2020**, *10*, 3707.
(68) Hsu, K. F.; Wu, C. L.; Huang, S. C.; Wu, C. M.; Hsiao, J. R.; Yo, Y.; Chen, Y. H.; Shiau, A. L.; Chou, C. Y. Cathepsin L Mediates Resveratrol-Induced Autophagy and Apoptotic Cell Death in Cervical Cancer Cells. *Autophagy* **2009**, *5*, 451.
(69) Eltouny, N.; Ariya, P. A. Competing Reactions of Selected Atmospheric Gases on Fe3O4 Nanoparticles Surfaces. *Phys. Chem. Chem. Phys.* **2014**, *16*, 23056.
(70) Tanwar, K.; Gyan, D. S.; Bhattacharya, S.; Vitta, S.; Dwivedi, A.; Maiti, T. Enhancement of Thermoelectric Power Factor by

https://doi.org/10.1021/acs.chemmater.2c03574
Chem. Mater. 2023, 35, 2439−2455

Inducing Octahedral Ordering in La2-XSrxCoFe O6 Double Perovskites. *Phys. Rev. B* **2019**, *99*, No. 174105.
(71) Hastuti, E.; Subhan, A.; Amonpattaratkit, P.; Zainuri, M.; Suasmoro, S. The Effects of Fe-Doping on MnO2: Phase Transitions, Defect Structures and Its Influence on Electrical Properties. *RSC Adv.* **2021**, *11*, 7808.
(72) Wang, T.; Zhang, S.; Yan, X.; Lyu, M.; Wang, L.; Bell, J.; Wang, H. 2-Methylimidazole-Derived Ni-Co Layered Double Hydroxide Nanosheets as High Rate Capability and High Energy Density Storage Material in Hybrid Supercapacitors. *ACS Appl. Mater. Interfaces* **2017**, *9*, 15510.
(73) Liu, T.; Guo, Y. F.; Yan, Y. M.; Wang, F.; Deng, C.; Rooney, D.; Sun, K. N. CoO Nanoparticles Embedded in Three-Dimensional Nitrogen/Sulfur Co-Doped Carbon Nanofiber Networks as a Bifunctional Catalyst for Oxygen Reduction/Evolution Reactions. *Carbon N. Y.* **2016**, *106*, 84.
(74) Haber, V.; Ptáček, P. XPS Study of Metal Complexes with an Unsymmetrical Tetradentate Schiff Base. *Inorg. Chim. Acta* **1991**, *179*, 267.
(75) Sun, Y.; Ren, X.; Sun, S.; Liu, Z.; Xi, S.; Xu, Z. J. Engineering High-Spin State Cobalt Cations in Spinel Zinc Cobalt Oxide for Spin Channel Propagation and Active Site Enhancement in Water Oxidation. *Angew. Chem. Int. Ed.* **2021**, *60*, 14536.
(76) Istomin, S. Y.; Tyablikov, O. A.; Kazakov, S. M.; Antipov, E. V.; Kurbakov, A. I.; Tsirlin, A. A.; Hollmann, N.; Chin, Y. Y.; Lin, H. J.; Chen, C. T.; Tanaka, A.; Tjeng, L. H.; Hu, Z. An Unusual High-Spin Ground State of Co3+ in Octahedral Coordination in Brownmillerite-Type Cobalt Oxide. *Dalton Trans.* **2015**, *44*, 10708.
(77) Brown, D. G.; Weser, U. XPS Spectra of Spin-Triplet Cobalt(III) Complexes. *Z. Naturforsch. B* **1979**, *34*, 1468.
(78) Vaz, C. A. F.; Prabhakaran, D.; Altman, E. I.; Henrich, V. E. Experimental Study of the Interfacial Cobalt Oxide in Co3 O 4/α-Al22 O3 (0001) Epitaxial Films. *Phys. Rev. B Condens. Matter Mater. Phys.* **2009**, *80*, No. 155457.
(79) Coutrim, L. T.; Bittar, E. M.; Stavale, F.; Garcia, F.; Baggio-Saitovitch, E.; Abbate, M.; Mossanek, R. J. O.; Martins, H. P.; Tobia, D.; Pagliuso, P. G.; Bufaiçal, L. Compensation Temperatures and Exchange Bias in La1.5Ca0.5CoIrO6. *Phys. Rev. B* **2016**, *93*, No. 174406.
(80) Sharannia, M. P.; Kayser, P.; Pillai, S. S.; Kennedy, B. J.; Avdeev, M.; Nirmala, R.; Santhosh, P. N. Observation of Nd Ordering in a Novel Double Perovskite Nd2MgRuO6 with Weak Exchange Interaction at B-Site. *J. Solid State Chem.* **2018**, *259*, 73.
(81) Zhang, Y.; Zhang, B.; Li, S.; Zhu, J.; Wu, B.; Wang, J.; Ren, Z. Cryogenic Magnetic Properties and Magnetocaloric Effects (MCE) in B-Site Disordered RE2CuMnO6 (RE = Gd, Dy, Ho and Er) Double Perovskites (DP) Compounds. *Ceram. Int.* **2021**, *47*, 18205.
(82) Silva-Santana, M. C.; Dasilva, C. A.; Barrozo, P.; Plaza, E. J. R.; De Los Santos Valladares, L.; Moreno, N. O. Magnetocaloric and Magnetic Properties of SmFe0.5Mn0.5O3 Complex Perovskite. *J. Magn. Magn. Mater.* **2016**, *401*, 612.
(83) Laguna-Marco, M. A.; Arias-Egido, E.; Cuartero, V.; Herrero-Albillos, J.; Kayser, P.; Alonso, J. A.; Fabbris, G.; Haskel, D.; Irifune, T. Probing the Tunability of Magnetism with External Pressure in Metastable Sr2NiIrO6 Double Perovskite. *Phys. Rev. B* **2022**, *105*, No. 064421.
(84) Das, M.; Roy, S.; Khan, N.; Mandal, P. Giant Magnetocaloric Effect in an Exchange-Frustrated GdCrTiO5 Antiferromagnet. *Phys. Rev. B* **2018**, *98*, No. 104420.
(85) Madhogaria, R. P.; Das, R.; Clements, E. M.; Kalappattil, V.; Phan, M. H.; Srikanth, H.; Dang, N. T.; Kozlenko, D. P.; Bingham, N. S. Evidence of Long-Range Ferromagnetic Order and Spin Frustration Effects in the Double Perovskite La2CoMnO6. *Phys. Rev. B* **2019**, *99*, No. 104436.
(86) Goto, M.; Oguchi, T.; Shimakawa, Y. Geometrical Spin Frustration and Monoclinic-Distortion-Induced Spin Canting in the Double Perovskites Ln2LiFeO6(Ln = La, Nd, Sm, and Eu) with Unusually High Valence Fe5+. *J. Am. Chem. Soc.* **2021**, *143*, 19207.
(87) García-Hernández, M.; Martínez, J. L.; Martínez-Lope, M. J.; Casais, M. T.; Alonso, J. A. Finding Universal Correlations between Cationic Disorder and Low Field Magnetoresistance in FeMo Double Perovskite Series. *Phys. Rev. Lett.* **2001**, *86*, 2443.
(88) Majumder, S.; Tripathi, M.; Raghunathan, R.; Rajput, P.; Jha, S. N.; de Souza, D. O.; Olivi, L.; Chowdhury, S.; Choudhary, R. J.; Phase, D. M. Mapping the Magnetic State as a Function of Antisite Disorder in Sm2NiMnO6 Double Perovskite Thin Films. *Phys. Rev. B* **2022**, *105*, No. 024408.
(89) Moon, J. Y.; Kim, M. K.; Oh, D. G.; Kim, J. H.; Shin, H. J.; Choi, Y. J.; Lee, N. Anisotropic Magnetic Properties and Giant Rotating Magnetocaloric Effect in Double-Perovskite T B2CoMn O6. *Phys. Rev. B* **2018**, *98*, No. 174424.
(90) Moon, J. Y.; Kim, M. K.; Choi, Y. J.; Lee, N. Giant Anisotropic Magnetocaloric Effect in Double-Perovskite Gd2CoMnO6 Single Crystals. *Sci. Rep.* **2017**, *7*, 16099.
(91) Krishna Murthy, J.; Devi Chandrasekhar, K.; Mahana, S.; Topwal, D.; Venimadhav, A. Giant Magnetocaloric Effect in Gd2NiMnO6 and Gd2CoMnO6 Ferromagnetic Insulators. *J. Phys. D Appl. Phys.* **2015**, *48*, No. 355001.
(92) Pässler, R. Non-Debye Heat Capacity Formula Refined and Applied to GaP, GaAs, GaSb, InP, InAs, and InSb. *AIP Adv.* **2013**, *3*, No. 082108.
(93) Yang, Z.; Zhang, H.; Bai, M.; Li, W.; Huang, S.; Ruan, S.; Zeng, Y. J. Large Magnetocaloric Effect in Gadolinium Borotungstate Gd3BWO9. *J. Mater. Chem. C* **2020**, *8*, 11866.
(94) Vasile, R. L.; Godoy, A. A.; Puente Orench, I.; Nemes, N. M.; De La Peña O'Shea, V. A.; Gutiérrez-Puebla, E.; Martínez, J. L.; Monge, M. Á.; Gándara, F. Influence of the Synthesis and Crystallization Processes on the Cation Distribution in a Series of Multivariate Rare-Earth Metal-Organic Frameworks and Their Magnetic Characterization. *Chem. Mater.* **2022**, *34*, 7029−7041.
(95) He, C.; Zheng, H.; Mitchell, J. F.; Foo, M. L.; Cava, R. J.; Leighton, C. Low Temperature Schottky Anomalies in the Specific Heat of LaCoO 3: Defect-Stabilized Finite Spin States. *Appl. Phys. Lett.* **2009**, *94*, 102514.
(96) Arrott, A.; Noakes, J. E. Approximate Equation of State for Nickel near Its Critical Temperature. *Phys. Rev. Lett.* **1967**, *19*, 786−789.
(97) Sahoo, R. C.; Das, S.; Nath, T. K. Role of Gd Spin Ordering on Magnetocaloric Effect and Ferromagnetism in Sr Substituted Gd2CoMnO6 Double Perovskite. *J. Appl. Phys.* **2018**, *124*, 103901.
(98) Zhang, L.; Menzel, D.; Jin, C.; Du, H.; Ge, M.; Zhang, C.; Pi, L.; Tian, M.; Zhang, Y. Critical Behavior of the Single-Crystal Helimagnet MnSi. *Phys. Rev. B-Condens. Matter Mater. Phys.* **2015**, *91*, No. 024403.
(99) Jia, Y.; Cheng, Y.; Wang, H.; Zhang, Z.; Li, L. Magnetocaloric Properties and Critical Behavior in Double Perovskite RE2CrMnO6 (RE = La, Pr, and Nd) Compounds. *Ceram. Int.* **2020**, *46*, 25043.
(100) Yang, X.; Pan, J.; Liu, S.; Yang, M.; Cao, L.; Chu, D.; Sun, K. Critical Behavior and Anisotropic Magnetocaloric Effect of the Quasi-One-Dimensional Hexagonal Ferromagnet PrCrGe3. *Phys. Rev. B* **2021**, *103*, No. 104405.
(101) Kouvel, J. S.; Fisher, M. E. Detailed Magnetic Behavior of Nickel near Its Curie Point. *Phys. Rev.* **1964**, *136*, A1626.
(102) Li, Y.; Lv, Q.; Feng, S.; Ur Rehman, K. M.; Kan, X.; Liu, X. A Comparative Investigation of B-Site Ordering and Structure, Magnetic, Magnetocaloric Effect, Critical Behavior in Double Perovskite Nd2BMnO6 (B = Co and Ni). *Ceram. Int.* **2021**, *47*, 32599.
(103) Tillaoui, S.; El Boubekri, A.; Essoumhi, A.; Sajieddine, M.; Hlil, E. K.; Moubah, R.; Sahlaoui, M.; Razouk, A.; Lassri, H. Structural, Magnetic, Magnetocaloric Properties and Critical Behavior of La0.62Nd0.05Ba0.33MnO3 Elaborated by Co-Precipitation Process. *Mater. Sci. Eng. B Solid-State Mater. Adv. Technol.* **2021**, *266*, No. 115052.
(104) Mondal, S.; Midya, A.; Patidar, M. M.; Ganesan, V.; Mandal, P. Magnetic and Magnetocaloric Properties of Layered van Der Waals CrCl3. *Appl. Phys. Lett.* **2020**, *117*, No. 092405.

(105) Zhang, Y.; Li, H.; Dan Guo; Hou, L.; Li, X.; Ren, Z.; Wilde, G. Cryogenic Magnetic Properties and Magnetocaloric Performance in Double Perovskite Pr2NiMnO6 and Pr2CoMnO6 Compounds. *Ceram. Int.* **2018**, *44*, 20762.
(106) Barclay, J. A.; Steyert, W. A. Materials for Magnetic Refrigeration between 2 K and 20 K. *Cryogenics* **1982**, *22*, 73.
(107) Shinde, K. P.; Lee, E. J.; Manawan, M.; Lee, A.; Park, S. Y.; Jo, Y.; Ku, K.; Kim, J. M.; Park, J. S. Structural, Magnetic, and Magnetocaloric Properties of R2NiMnO6 (R = Eu, Gd, Tb). *Sci. Rep.* **2021**, *11*, 20206.
(108) Krishnamurthy, J.; Venimadhav, A. Magnetic Field-Induced Metamagnetic, Magnetocaloric and Pyrocurrent Behaviors of Eu2CoMnO6. *J. Magn. Magn. Mater.* **2020**, *500*, No. 166387.
(109) Mazumdar, D.; Das, I. Role of 3d-4f Exchange Interaction and Local Anti-Site Defects in the Magnetic and Magnetocaloric Properties of Double Perovskite Ho2CoMnO6compound. *J. Appl. Phys.* **2021**, *129*, No. 063901.
(110) Pecharsky, A. O.; Gschneidner, K. A.; Pecharsky, V. K. The Giant Magnetocaloric Effect of Optimally Prepared Gd5Si2Ge2. *J. Appl. Phys.* **2003**, *93*, 4722−4728.
(111) Franco, V.; Conde, A. Scaling Laws for the Magnetocaloric Effect in Second Order Phase Transitions: From Physics to Applications for the Characterization of Materials. *Int. J. Refrig.* **2010**, *33*, 465.
(112) Li, L.; Xu, P.; Ye, S.; Li, Y.; Liu, G.; Huo, D.; Yan, M. Magnetic Properties and Excellent Cryogenic Magnetocaloric Performances in B-Site Ordered RE2ZnMnO6 (RE = Gd, Dy and Ho) Perovskites. *Acta Mater.* **2020**, *194*, 354.
(113) Yin, Y.; Shi, F.; Liu, G. Q.; Tan, X.; Jiang, J.; Tiwari, A.; Li, B. Spin-Glass Behavior and Magnetocaloric Properties of High-Entropy Perovskite Oxides. *Appl. Phys. Lett.* **2022**, *120*, No. 082404.
(114) Bhatti, I. N.; Bhatti, I. N. Spin Glass Behavior and Critical Analysis across the Magnetic Phase Transition in Gd2CoMnO6: Dc Magnetization and Ac Susceptibility Study. *Curr. Appl. Phys.* **2022**, *39*, 97−106.
(115) Kitanovski, A. Energy Applications of Magnetocaloric Materials. *Adv. Energy Mater.* **2020**, *10*, No. 1903741.

https://doi.org/10.1021/acs.chemmater.2c03574
Chem. Mater. 2023, 35, 2439−2455